Enhanced photoelectrochemical performance of Z-scheme g-C$_3$N$_4$/BiVO$_4$ photocatalyst

Javad Safaei[a,*], Habib Ullah[b,*], Nurul Aida Mohamed[a], Mohamad Firdaus Mohamad Noh[a], Mohd Fairus Soh[a], Asif A. Tahir[b], Norasikin Ahmad Ludin[a], Mohd Adib Ibrahim[a], Wan Nor Roslam Wan Isahak[c], Mohd Asri Mat Teridi[a,*]

[a] *Solar Energy Research Institute, National University of Malaysia, 43600, Bangi, Selangor, Malaysia*
[b] *Environment and Sustainability Institute, University of Exeter, Penryn Campus, Penryn, Cornwall, TR10 9FE, United Kingdom*
[c] *Department of Chemical and Process Engineering, Faculty of Engineering and Build Environment, National University of Malaysia, 43600, Bangi, Selangor, Malaysia*

ARTICLE INFO

ABSTRACT

BiVO$_4$ is a considerably promising semiconductor for photoelectrochemical water splitting due to its stability, low cost and moderate band gap. In this research, g-C$_3$N$_4$ was proposed in Z-scheme configuration which boosted the performance of BiVO$_4$ up to four times. The experimental observations were counterchecked with Density Functional Theory (DFT) simulations. A TiO$_2$/BiVO$_4$ heterojunction was developed and its performance was compared with that of g-C$_3$N$_4$/BiVO$_4$. The photocurrent for g-C$_3$N$_4$/BiVO$_4$ was 0.42 mAcm^{-2} at 1.23 V vs. RHE which was the highest among g-C$_3$N$_4$ based Z-scheme heterojunction devices. Lower charge transfer resistance, higher light absorption and more oxygen vacancy sites were observed for the g-C$_3$N$_4$ based heterojunction. The simulated results attested that g-C$_3$N$_4$ and BiVO$_4$ formed a van der Waals type heterojunction, where an internal electric field facilitated the separation of electron/hole pair at g-C$_3$N$_4$/BiVO$_4$ interface which further restrained the carrier recombination. Both the valence and conduction band edge positions of g-C$_3$N$_4$ and BiVO$_4$ changed with the Fermi energy level. The resulted heterojunction had small effective masses of electrons (0.01 m$_e$) and holes (0.10 m$_e$) with ideal band edge positions where both CBM and VBM were well above and below the redox potential of water.

1. Introduction

BiVO$_4$ has received extensive attention due to its moderate band gap, good stability and high activity for oxygen evolution which is a rate determining step in photoelectrochemical (PEC) water splitting [1]. It primarily exists in three different crystalline polymorphs, namely, orthorhombic pucherite, tetragonal dreyerite, and monoclinic clinobisvanite [2]. The photocatalytic activity and surface reaction is highly dependent on the phase and crystal orientation of a semiconductor oxide [3–5]. For instance, the tetragonal BiVO$_4$ possesses a band gap of 2.9 eV and predominantly absorbs UV light, while the monoclinic clinobisvanite phase exhibits a much higher photocatalytic activity due to its favourable band gap (2.4–2.5 eV) in the visible region [6]. Monoclinic clinobisvanite phase, however, has certain drawbacks such as low conduction band minimum position, poor charge transport properties and high recombination rate of photoelectrons, restraining its overall efficiency [7].

Numerous strategies have been adopted to enhance the performance of BiVO$_4$. The enhancement can be obtained by doping or utilizing oxygen evolution reaction (OER) catalyst. Cobalt-phosphate, iron oxyhydroxide and nickel oxyhydroxide were introduced as OER catalyst to improve the surface kinetics [8–11] while tungsten and molybdenum were deployed to increase charge carrier densities [6,12–15]. Morphology control and facet modifications were utilized to investigate the charge separation and photocatalytic behaviour of BiVO$_4$ [16–21]. Zero-dimensional (0D) Quantum-sized BiVO$_4$ (5–20 nm) demonstrated higher PEC activities compared with those of nanoparticles (3D) ∼ 200 nm due to their superior life time and elevated conduction band [16,17].

Another noteworthy strategy is to develop heterojunctions with the implementation of other types of semiconductors. The development of heterojunction with BiVO$_4$ suppresses its charge recombination by improving the charge transport properties. Furthermore, this strategy engenders the possibility of electronic band structure widening of BiVO$_4$ to undergo hydrogen evolution reaction (HER). It also broadens BiVO$_4$'s light absorption due to the implementation of diverse types of

---

materials with unidentical band gaps. Several types of heterojunctions can be constructed by employing two semiconductors, depending on their valence and conduction band edge positions. We have explained four diverse types of heterojunctions in our previous report [22]. Yet the application of type (II) heterojunction have been more prominent in previous researches, for the photogenerated electrons and holes in BiVO$_4$ tend to step down to a lower energy level of TiO$_2$ nanostructures or WO$_3$, contributing to HER on counter electrode and OER on BiVO$_4$ (Fig. S1) [9,22–29].

The graphitic carbon nitride (g-C$_3$N$_4$) has proved highly suitable for its oxygen and hydrogen evolution properties, moderate band gap of 2.7 eV, high photoelectrochemical and thermal stability, environmentally friendly properties, and its abundance in nature [30–32]. The more negative conduction band edge potential of g-C$_3$N$_4$, compared with the state of the art photocatalysts such as BiVO$_4$, TaON, WO$_3$, TiO$_2$, Fe$_2$O$_3$, ZnO, etc. enables it to form type (II) or Z-scheme heterojunction [33–35]. Despite its capability to absorb light in the visible range, the photocurrent of g-C$_3$N$_4$ is limited to only a few microamperes due to its high recombination rate of the photogenerated electron/hole pairs [33]. Although, the utilization of g-C$_3$N$_4$ as a hole extraction layer on top of TiO$_2$ [36] and ZnO [37] has proved successful, the development of thin film utilizing g-C$_3$N$_4$ as electron extraction layer is still in its preliminary stages.

If the host material, that is, the semiconductor deposited on FTO for two semiconductor heterojunction thin films in contact, has its conduction band above the water reduction potential and if the guest material has its valence band below the water oxidation potential, Z-scheme will be formed, leading to HER and OER at the counter electrode and guest material, respectively [22,38]. In order to obtain similar or higher order of PEC enhancement for BiVO$_4$, compared with TiO$_2$ or WO$_3$ nanostructures, one needs to employ semiconductors in Z-scheme with BiVO$_4$ due to its high efficiency in charge transportation and redox ability [33].

In our previous study, Selenium (Se) was deployed as a host material in Z-scheme to enhance the performance of BiVO$_4$ up to three times [22]. In another study by Wang et al. Z-scheme was constructed, using g-C$_3$N$_4$ and WO$_3$ (see Fig. 1) [38]. Even though Z-scheme provided a much higher boost for WO$_3$ compared with type (II) heterojunction, the overall performance of Z-scheme was still lower due to low photocurrent of planar WO$_3$ in relation to nanostructures such as WO$_3$ nanorods (WO$_3$-NRs) [27,38].

For BiVO$_4$, three methods of electrodeposition were developed, involving the intermediary phase of V$_2$O$_5$ that needed to be removed in 1 M KOH (~pH 13) aqueous solutions [10,39,40]. To fabricate heterojunctions with BiVO$_4$, using facile electrodeposition methods, the utilized semiconductor must be stable in strong basic/alkaline aqueous

solutions. The extensively deployed WO$_3$ limits the fabrication methods due to the instability of WO$_3$ in basic aqueous media. WO$_3$ forms sodium tungstate due to more stable phase of WO$_4^{-2}$ in the pH of 8 and above (see Reaction (1)) [41]. It is necessary to mention that extremely thin layer of BiVO$_4$ (~40 nm) did not require basic/alkaline treatment [27], although this thickness is operational only on WO$_3$-NRs nanostructures which are costly to fabricate in comparison with planar structures [9,42].

$$WO_3 + 2NaOH \rightarrow Na_2WO_4 + H_2O \qquad (1)$$

The present research addresses two types of heterojunctions, comprised of g-C$_3$N$_4$/BiVO$_4$ and TiO$_2$/BiVO$_4$, where the former has superior efficiency. Various experimental methods have been utilized to investigate the performance of these heterojunctions. The experimental results, counterchecked with first principle density functional theory (DFT) simulations, confirmed that g-C$_3$N$_4$/BiVO$_4$ forms a van der Waals type heterojunction (Z-scheme), where an internal electric field facilitates the separation of electron−hole pair at the g-C$_3$N$_4$/BiVO$_4$ interface which further restrain the carrier recombination.

2. Methods

2.1. Synthesis of g-C$_3$N$_4$ thin film

Fluorine doped Tin Oxide (FTO TEC 8 Ω/cm^2, Pilkington) was deployed as substrate. Before deposition, FTO was respectively washed in acetone, ethanol and deionised water for ten minutes each, in ultrasonic bath, and dried with flow of nitrogen. The standard pyrolysis of urea was utilized to synthesize g-C$_3$N$_4$ in box furnace. Three grams of Urea (3 g; 99%, Aldrich), was poured in 50 ml alumina crucible with its lid on, with the temperature gradually rising to 520 °C in 15 min and remaining steady then for 15 min. Next the crucible was left in the furnace until it cooled down to the temperature of 400 °C before it was taken out of furnace and placed at room temperature. The obtained fine yellow powder (30–40 mg) was dispersed in deionised water and washed by centrifugation and ultrasonication three consecutive times to remove any extra organic compound. Then it was dried overnight at 100 °C in an oven and dispersed in methanol, deploying ultrasonic bath for 10 min with a concentration of 0.5 mg/ml. Before deposition of g-C$_3$N$_4$ thin film, the suspension was ultrasonicated for one minute to attain uniform suspension. For deposition of one-layer g-C$_3$N$_4$ [g-C$_3$N$_4$ (1 L)] thin film, 10 micro liter of the suspension was spun on the precleaned FTO with speed of 2500 rpm, acceleration of 500 rpm/s and duration of 10 s. The g-C$_3$N$_4$ thin film was left at room temperature for five minutes to partially dry before performing another spin coating process for depositing second [g-C$_3$N$_4$ (2 L)] and third layer [g-C$_3$N$_4$

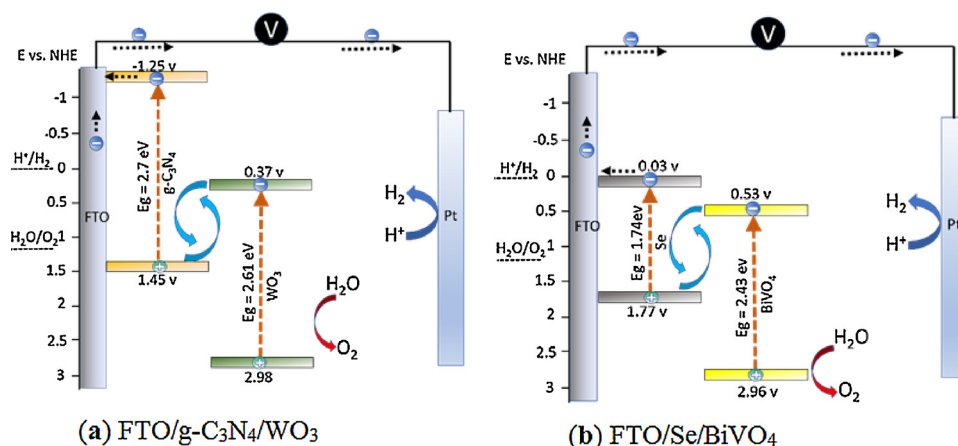**Fig. 1.** Z-schemes, developed comprising g-C$_3$N$_4$/WO$_3$ (a) [38] and Se/BiVO$_4$ (b) [22]. In these heterojunction thin-film structures, the electrons from conduction band of g-C$_3$N$_4$ or Se directly contributed to HER while holes from valence band of WO$_3$ or BiVO$_4$ contributed to OER.

(3 L)]. Finally, g-C$_3$N$_4$ thin films were dried at 350 °C degrees on hot plate for 30 min.

2.2. Synthesis of TiO$_2$ thin film

TiO$_2$ thin film was fabricated by using commercial paste (18 NR-T, Dyesol) with three different concentrations of 5, 10 and 20 mg/mL in ethanol to deposit respectively different thickness of TiO$_2$ namely, TiO$_2$(A), TiO$_2$(B) and TiO$_2$(C) (See Supporting information Fig. S1 for TiO$_2$ nanoparticles). Subsequently, 10 µL of suspension was spun with speed of 2500 rpm, acceleration of 500 rpm/s with duration of 10 s. All TiO$_2$ thin films were annealed in a tube furnace at 500° for 2 h with a ramping rate of 0 °C/min.

2.3. Synthesis of BiVO$_4$, TiO$_2$/BiVO$_4$, and g-C$_3$N$_4$/BiVO$_4$ thin films

The electrodeposition method, developed by Seabold et al. [10] was used to synthesize BiVO$_4$ with a slight modification. Briefly, 10 mM bismuth nitrate pentahydrate of Bi(NO$_3$)$_2$·5H$_2$O (98%, Aldrich) and 35 mM vanadium oxide sulphate hydrate VSO$_5$·xH$_2$O (97%, Aldrich) were stirred in 1 M of nitric acid (68%, Aldrich) for 10 min. Then, sodium acetate (ACS Reag, Merck) was used to stabilize the solution to (PH ~ 5.1) and to (PH ~ 4.7) with a few drops of nitric acid. Electrodeposition process was carried out at 50° under a potential of 1.9 V vs. Ag/AgCl for 10 min, with FTO as working and platinum as counter electrode. After the electrodeposition, the blackish/yellowish samples, identified as Bi−V−O, were rinsed with DI water and left at room temperature to dry. Afterwards the samples were annealed in a tube furnace at

2.4. Characterizations

The electrochemical properties of the prepared samples were examined on Autolab potentiostat/galvanostat PGSTAT 204 at room temperature, utilizing three electrode configurations with Ag/AgCl (3 M NaCl) as reference electrode and 0.5 M Na$_2$SO$_4$ (PH ~ 7.0) as electrolyte. Potentials were converted to Reversible Hydrogen Electrode (RHE) by using Eq. (1).

$$E_{RHE} = E_{Ag/Agcl} + 0.059 \, pH + E_{0 \, Ag/Agcl} \, (0.1976) \qquad (1)$$

Xenon lamp with 100 mW/cm^2 intensity was used as solar light simulator. The electrochemical fitting of Nyquist plots was analysed with the application of Nova Software. The optical properties of the samples were analysed by UV–vis absorption spectrophotometer, Perkin Elmer Lambda 950. The physical and morphological properties of samples were characterised with X-ray Diffraction (XRD), Field Emission Scanning Electron Microscopy (FESEM) (FE-SEM Supra VP 55) and Atomic Force Microscopy (AFM) (NanosurfeasyScan 2). The X-ray Photoelectron Spectroscopy (XPS) with Al Ka X-ray gun was implemented to analyse the chemical bonding and valence band structure. The reference value of carbon 285 eV was considered in this analysis. Photoluminescence spectra were analysed (via PL Edinburgh Instruments) to measure the radiative recombination of the samples at excitation wavelength of 300 nm.

2.5. Theoretical methods

First principle DFT calculations were performed on QuantumWise-ATK [43] and results were visualized on VESTA and Virtual NanoLab Version 2017.1 [44]. Clinobisvanite BiVO$_4$ was used as such with Hall symmetry space group of I2/b [45]. The lattice parameters of the 24 atoms unit cell were optimized and a supercell (2 × 2 × 2) was then constructed for the fabrication of BiVO$_4$(001) slab. For the slab model calculations of surface energies and band edge positions, thickness of the slab was kept by four primitive unit cells of BiVO$_4$ (10 Å thick

having 96 atoms) to ensure that the centre of the slab can be regarded as the bulk phase. A vacuum space of about 10 Å was inserted between slabs to eliminate the fictitious interaction between the periodically repeating slabs. The (001) termination possesses low surface energy and represents the most probable surface termination [18]. Stability of these different slabs are confirmed from their positive surface formation energy and electrostatic potential; details of surface formation energy is given in Eq. (S1), Table S1 and Fig. S2 of the Supporting information. Both single layer and bulk g-C$_3$N$_4$ were considered for simulations: the structure of the single layer g-C$_3$N$_4$ is portrayed in Fig. 13, while that of bulk is presented in Fig. S11 and Table S2 of the Supporting information. Generalized Gradient Approximation (GGA) with the Perdew–-Burke–Ernzerhof (PBE) exchange-correlation functional and Double Zeta Polarized (DZP) basis set were employed for the structural and energy optimization as a consequence of their superiority to hybrid pseudopotentials [46]. Moreover, linear combination of atomic orbitals (LCAO) method was applied to Bi, V, Ti, C, N, H, and O atoms [47]. A 7 × 7 × 3 Monkhorst-Pack k-grid with the energy cutoff of 1200 eV was deployed for the BiVO$_4$ unit cell while a 5 × 5 × 1 k-point mesh was utilized for its slabs. 7 × 7 × 7 Monkhorst-Pack k-grid with the energy cutoff of 900 eV was implemented for monolayer g-C$_3$N$_4$, and 5 × 5 × 1 k-point mesh with 1200 eV cutoff energy was utilized for g-C$_3$N$_4$/BiVO$_4$(001) heterostructure. The band structure calculations were performed with TB09LDA functional of meta-GGA that could accurately reproduce the experimental band gaps. Tran and Blaha assert that this accuracy is due to the use of local density ρ(r) (as in LDA), the gradient of the density ∇ρ(r) (as in GGA), and the kinetic-energy density τ(r) [48]. We have fitted the c-parameter of Tran and Blaha XC functional's equation to reproduce optimally the experimental band gaps [48]. Density of states (DOS), partial density of states (PDOS), band structure and effective masses of photogenerated electrons and holes were also calculated. The DFT occupied and unoccupied DOS were considered as the VB and CB edges, respectively and then separated by an energy equal to the known optical band gap [49].

3. Results and discussion

3.1. Structural analysis

XRD plots of g-C$_3$N$_4$ and TiO$_2$ along with their corresponding BiVO$_4$ heterojunctions are illustrated in Figs. 3 and 4, respectively. The peaks of TiO$_2$ and BiVO$_4$ suggest respectively a high crystalline phase of anatase and monoclinic sheet [10,50]. No extra peak for anatase TiO$_2$ was observed except for the two highest peaks ca. at (101) and (200) due to insufficient thickness of TiO$_2$. In case of g-C$_3$N$_4$ powder, two peaks ca. at (100) and (002) planes were found corresponding to interplanar separation of g-C$_3$N$_4$ sheets and interlayer stacking of the aromatic systems, respectively [30].

The g-C$_3$N$_4$/BiVO$_4$ thin film had sharper and clearer peaks compared with TiO$_2$/BiVO$_4$ thin film. This is confirmed by the appearance of (211) and (020) peaks and sharpening of (240) and (042) peaks (Figs. 3d and 4d). The increase in the intensity of (121), (040), (051), (042) and (161) peaks supports the fact that g-C$_3$N$_4$/BiVO$_4$ is better crystallized compared with TiO$_2$/BiVO$_4$. The Gaussian fit was performed on (121) peak and FWHM was found to be 0.346° and 0.263° for TiO$_2$/BiVO$_4$ and g-C$_3$N$_4$/BiVO$_4$, respectively. The crystallite size obtained from Scherrer formula was found to be 23.64 and 31.46 nm for TiO$_2$/BiVO$_4$ and g-C$_3$N$_4$/BiVO$_4$, respectively.

3.2. Morphology

The anodic electrodeposition of BiVO$_4$ involves co-precipitation of Bi^{3+} with V^{5+} that precipitates as amorphous Bi−V−O [51]. The initial morphology of host materials can highly affect the morphology of final crystalline heterojunction once the amorphous phase is annealed. This was also confirmed by Pihosh et al. [27] and Tong et al. [24] where the

anodic electrodeposition of amorphous Bi−V−O assumed the shape of WO$_3$ or TiO$_2$ nanostructures and established a core/shell structure by being covered around the nanorods.

A comparable phenomenon occurred in this research where the initial morphology of the substrate (planar g-C$_3$N$_4$ and TiO$_2$, in this case) transformed the final morphology of the heterojunction thin film (Fig. 5a–c). This is lucidly depicted in Fig. 5d–i where the morphology of pristine BiVO$_4$ electrodeposited on bare FTO entirely differs from that of TiO$_2$/BiVO$_4$ and g-C$_3$N$_4$/BiVO$_4$. This change of morphology highly depends on the deposition technique since other methods such as spin coating/drop coating of BiVO$_4$ on planar/nanostructured WO$_3$ [29,52] or TiO$_2$ [53] substrate have resulted in no morphological change between pristine BiVO$_4$ and its heterojunction. Since final morphology of our heterojunction structure highly depends on the morphology of host substrate, the fabrication of g-C$_3$N$_4$/BiVO$_4$ heterojunction on other morphologies of g-C$_3$N$_4$ such as nanorods/nanoflowers appears to be a promising field for further investigation.

3.3. Light absorption

Formation of g-C$_3$N$_4$/BiVO$_4$ and TiO$_2$/BiVO$_4$ caused a significant increase in light absorption compared with BiVO$_4$, illustrated in Fig. 6. Both g-C$_3$N$_4$/BiVO$_4$ and TiO$_2$/BiVO$_4$ demonstrated high absorbance below and above 500 nm. The higher absorbance of g-C$_3$N$_4$/BiVO$_4$ and TiO2/BiVO4, compared with BiVO$_4$ above 500 nm, does not contribute to photogenerated electrons, since BiVO$_4$ tends to transmit all that wavelength due to its band gap (Eg ~ 2.4 eV). Meanwhile, the lower wavelengths (500 nm) are effectively absorbed. Higher absorbance is noticeable for g-C$_3$N$_4$/BiVO$_4$ compared with TiO$_2$/BiVO$_4$ at the wavelengths shorter than 500 nm which can be one of the reasons of its superior performance compared with that of TiO$_2$/BiVO$_4$.

The higher light absorption of g-C$_3$N$_4$/BiVO$_4$ is due to the lower band gap of g-C$_3$N$_4$ (E$_g$ ~ 2.7 eV) compared with TiO$_2$ (E$_g$ ~ 3.3 eV) that tends to absorb larger portions of light. It is worth noting that larger grains of g-C$_3$N$_4$/BiVO$_4$ tend to increase its light trapping capability that, in turn, elevates its absorptivity [22,54–56]. This is also displayed in Fig. 2c where g-C$_3$N$_4$/BiVO$_4$ appears to be more opaque compared with TiO$_2$/BiVO$_4$.

3.4. XPS

Surface chemistry and valence band structure of the thin film heterojunctions were investigated by using XPS. The characteristic peaks of C1s bonding for g-C$_3$N$_4$ and g-C$_3$N$_4$/BiVO$_4$ are portrayed in Fig. 7a. The deconvolution peaks ca. at 285.0, 286.59, and 288.6 eV display the adventitious carbon sp^2 bonded (C−C) or (C=C) on the XPS instrument (reference value for carbon charging) [57,58], sp^3 hybridized C atom C−(N)$_3$ [57] and sp^2 C atoms bonded to N in (N−C=N) aromatic rings, respectively [59].

The N1s characteristic peaks of g-C$_3$N$_4$ and g-C$_3$N$_4$/BiVO$_4$ heterojunction are illustrated in Fig. 7b. The wide scan for g-C$_3$N$_4$ (Fig. S3) displays higher intensity of N1s peak compared with C1s, further
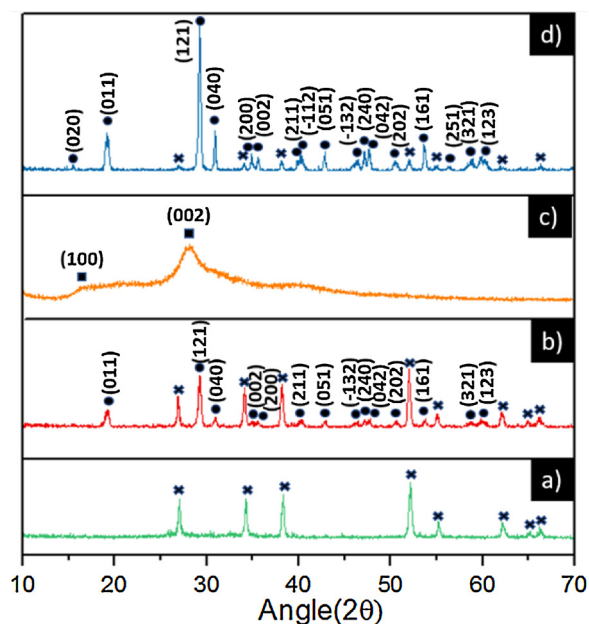

Fig. 3. XRD peaks for FTO (a), BiVO$_4$ (b), g-C$_3$N$_4$ (c) and g-C$_3$N$_4$/BiVO$_4$ (d).
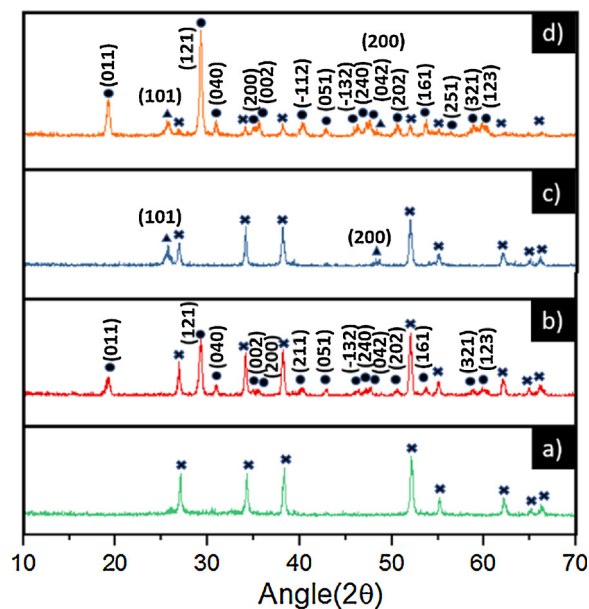
Fig. 4. XRD peaks for FTO (a), BiVO$_4$ (b), TiO$_2$ (c) and TiO$_2$/BiVO$_4$ (d).
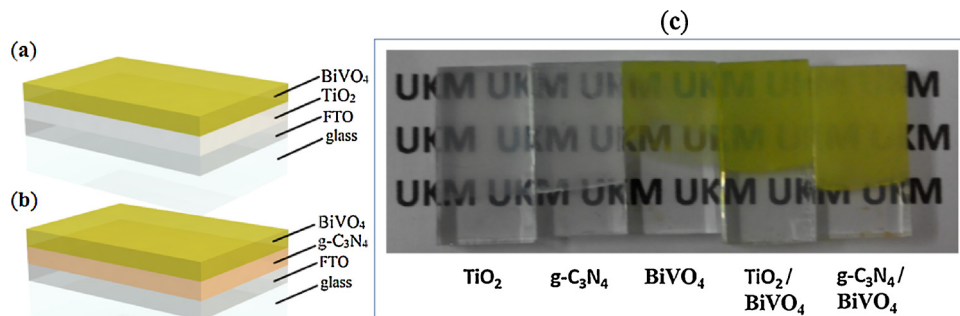
Fig. 2. 3D illustration of TiO$_2$/BiVO$_4$ (a) and g-C$_3$N$_4$/BiVO$_4$ (b) and actual fabricated thin films (c).
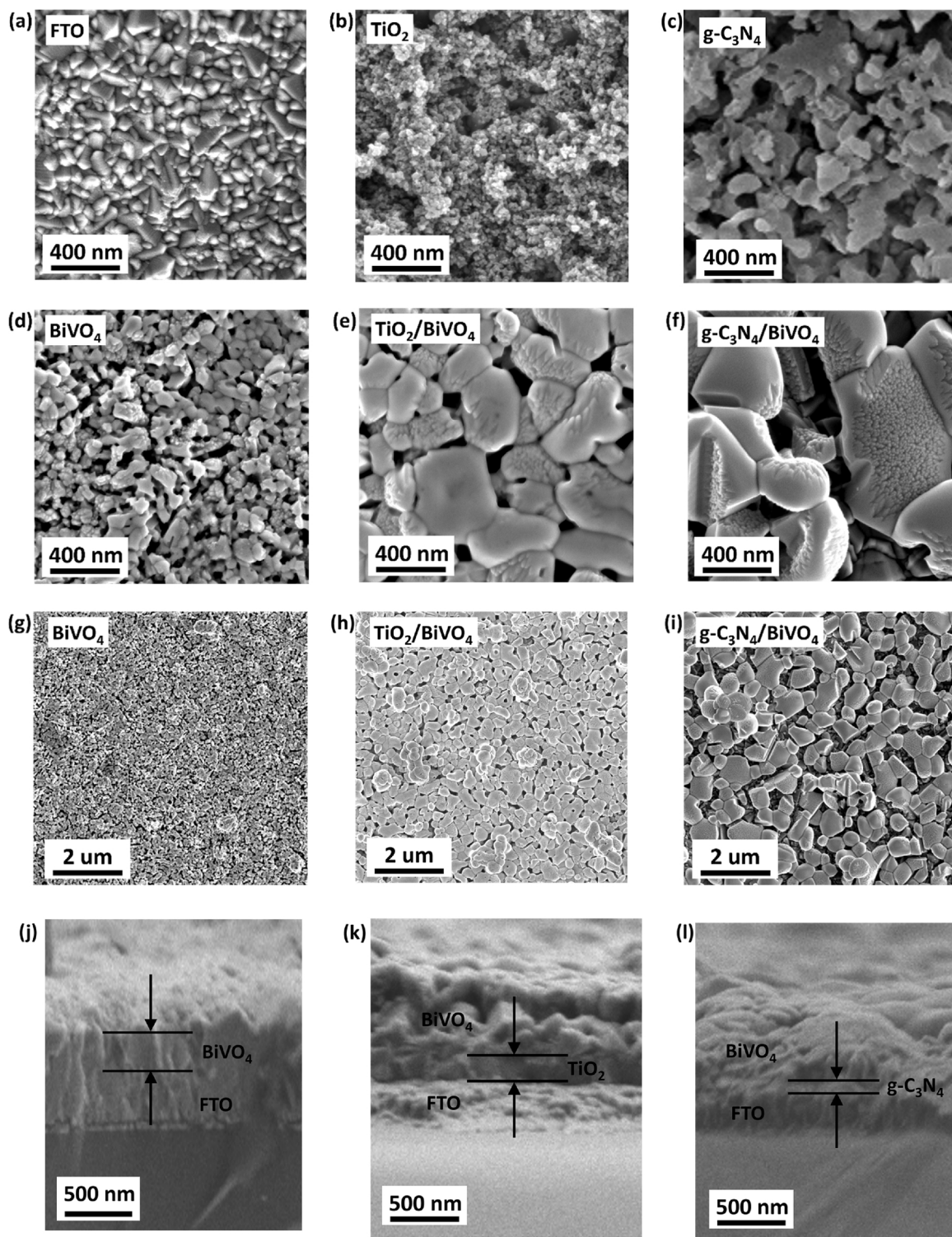
Fig. 5. FESEM images of pristine FTO (a), TiO_2 (b), g-C_3N_4 (c). FESEM surface images of $BiVO_4$ electrodeposited on FTO (d,g), on TiO_2 (e,h), on g-C_3N_4 (f,i). FESEM cross section images of $BiVO_4$ (j), $TiO_2/BiVO_4$ (k) and g-$C_3N_4/BiVO_4$ (l). These images affirm that the morphology of the host substrate can significantly affect the morphology of the electrodeposited $BiVO_4$.

confirming the formation of g-C_3N_4. The sp^2 hybridized bonding of nitrogen with carbon (C=N−C) in the framework of the heptazine unit, tertiary nitrogen bonded to three carbon atoms N−(C)$_3$, weak amino functional groups carrying hydrogen C−N−H caused by incomplete condensation and π-excitations ($\pi \rightarrow \pi^*$ transition), respectively appeared ca. at 399.06, 400.36, 401.51, and 406.07 eV. The C1s and N1s peaks for g-C_3N_4 were quenched for g-$C_3N_4/BiVO_4$ heterojunction due

to wrapping of g-C_3N_4 by $BiVO_4$ (Fig. 7a–b). This peak, nonetheless, was expected for adventitious carbon on XPS instruments that existed for g-$C_3N_4/BiVO_4$ heterojunction. A similar effect was observed in another report by Wang et al. where C1s peak at 284.6 and N1s peaks were quenched due to g-C_3N_4, being wrapped by WO_3 [38]. A commensurable effect can be observed for $TiO_2/BiVO_4$ heterojunction in Fig. 7c where both Ti2p 3/2 and Ti2p 1/2 peaks are heavily quenched
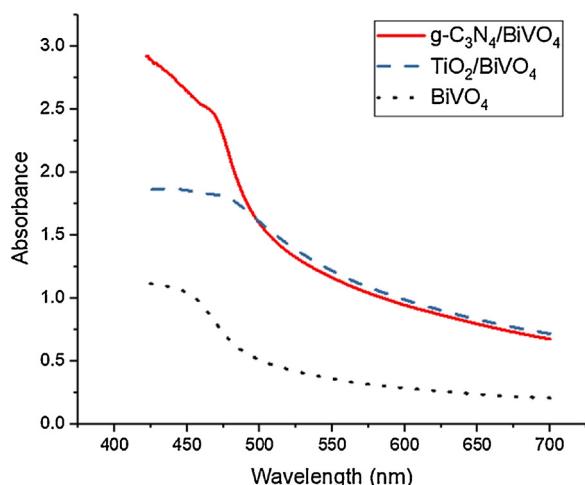
Fig. 6. Light absorption plots for $BiVO_4$, $TiO_2/BiVO_4$ and g-$C_3N_4/BiVO_4$.

by $BiVO_4$.

In Fig. 7d–e, the symmetric peaks of Bi4f 7/2, Bi4f 5/2, V2p 3/2 and V2p 1/2 bonds appear at 158.9, 164.23, 516.53, and 523.85 eV, respectively which underscore the presence of Bi^{3+} and V^{5+} state of $BiVO_4$. There is, nevertheless, a slight shift to higher energies for V2p 1/2 of $TiO_2/BiVO_4$ and a shift to lower energies for V2p 3/2 of g-$C_3N_4/BiVO_4$ compared with bare $BiVO_4$ (Fig. 7f–g). The shift to higher energies is congruous to that reported by Zalfani et al. for $TiO_2@BiVO_4$ photocatalyst where an up-shift for Bi4f and V2p displayed the oxidation of inherent V^{4+} to V^{5+} [58]. The shift, in the present research, to lower energies concords with other researches where a similar down-shift of V2p to lower binding energy was reported for hydrogen treated $BiVO_4$, $NaBH_4$ reduced $BiVO_4$ and $BiVO_4@g$-C_3N_4 photocatalyst, affirming the reduction of inherent V^{5+} to V^{4+} due to the presence of hydrogen element [60–63].

The shift of V2p to higher energies occasions the excess formation of V^{5+} that reduces the shielding effect on the bismuth due to smaller electronic cloud around V^{5+} and increases the electronic density of Bi4f for $TiO_2/BiVO_4$ (Fig. 7d). Contrarily, the shift towards lower energies implies the formation of V^{4+}, increasing the shielding effect on bismuth that reduces the electronic density around Bi4f for g-$C_3N_4/BiVO_4$ (Fig. 7d). The same effect was also investigated and explained by Zhang et al. for V^{4+} self-doped $BiVO_4$ where an increase in the electronic state was due to Bi4f [64].

The formation of V^{4+} state leads to the formation of oxygen vacancies that act as the centre of active catalytic sites and adsorption of superoxide O_2^- via atmospheric oxygen. The ratio of oxygen vacancy to lattice oxygen was found, using Gaussian fitting (Fig. 7h), and proved to be more for g-$C_3N_4/BiVO_4$ (1.33) compared with $TiO_2/BiVO_4$ (1.046). The higher ratio of adsorbed oxygen to lattice oxygen confirms more OH^- species can be attracted to the sites, further enhancing the catalytic performance.

In a nutshell, V^{4+} ions are made from the reduction of V^{5+} by hydrogen atoms, present in the interlayer of s-heptazine ring units of g-C_3N_4 that can generate oxygen vacancies which perform as active catalytic sites, with these catalytic sites adsorbing water molecules. Moreover, the carrier concentration is augmented due to the existence of self-doped V^{4+} further elaborated in later sections.

3.5. Band diagram

XPS, Mott-Schottky and UV–vis were performed to find the valence band maximum, Fermi level and conduction band minimum for the energy band diagram of bare semiconductors (Figs. S4–S7). The proposed heterojunctions are illustrated in Fig. 8, where TiO_2 and $BiVO_4$ form a Type (I) heterojunction while g-C_3N_4 and $BiVO_4$ comprise Type

(II) heterojunction. It is worth mentioning that the Fermi level shifts for two semiconductors when they interface one another, forming an overall band diagram (vide infra).

In the present research, type (I) heterojunction for $TiO_2/BiVO_4$ and type (II) heterojunction for g-$C_3N_4/BiVO_4$ can be further extended into a Z-scheme heterojunction under the application of a positive bias. The anodic photocurrent (to be further elaborated in the later sections of this paper) suggests oxidation reaction at $BiVO_4$ and reduction at the counter electrode. This implies that high energy electrons of TiO_2 and g-C_3N_4 directly reduce water at the counter electrode while the electrons at the conduction band energies of $BiVO_4$ are recombined with the holes at the valence band of TiO_2 and g-C_3N_4. Furthermore, the holes at the valence band of $BiVO_4$ surface are left to oxidize water. In both aforementioned heterojunctions, TiO_2 and g-C_3N_4 act as electron extraction layers as pathways to transfer electrons to the counter electrode as opposed to other structures where g-C_3N_4 acts as hole extraction layer [36,37].

3.6. PL spectra

The formation of heterojunction is proved from the decrease of PL radiative recombination at $BiVO_4$ and g-C_3N_4 (Fig. 9). The sharp peak in section (I), existent in all samples, suggests diffraction of the wavelength that occurs due to existence of FTO substrate and hence, it can be ignored. Although $BiVO_4$ photocatalyst presents one peak around ~520 nm [65], its thin-film photoelectrode behaves differently by having multiple peaks in sections II and III, presumably due to the scattering of light. However, the quench of radiative recombination, observed for two heterojunctions compared with bare $BiVO_4$, suggests successful formation of interface that facilitates charge transfer, hence, diminishing recombination. TiO_2 demonstrates the lowest PL intensity, attributable to recombination in singly ionized oxygen vacancy [66], with the g-C_3N_4 possessing its sharp characteristic fluorescence peak around 450 nm [67], being partially quenched after forming heterojunction structure (Fig. 9) [68,69].

3.7. Electrochemical properties

The Linear Sweep Voltammetry (LSV) was performed under back-illumination for dark and light to discover the photoelectrochemical response of the samples. The performance of g-$C_3N_4/BiVO_4$ and $TiO_2/BiVO_4$ thin films were optimized and the results are illustrated in Fig. 10a–b, demonstrating that the photocurrent of g-$C_3N_4/BiVO_4$ and $TiO_2/BiVO_4$ decreases when the thickness of g-C_3N_4 and TiO_2 increases. This occurs when some of the lights are blocked [70] by g-C_3N_4 and TiO_2 from reaching $BiVO_4$, generating less electron/hole pairs. Moreover, the increase in the thickness of g-C_3N_4 and TiO_2 presents high impedance in the path of electron/hole pairs [71] (to be elaborated under Fig. 12a–b), with this leading to the highest photocurrent of two thin films to be 0.42 and 0.22 mA for g-C_3N_4(1 L)/$BiVO_4$ and TiO_2(A)/$BiVO_4$, respectively.

The comparison of these two heterojunction photoanodes with that of pristine thin films of $BiVO_4$, TiO_2 and g-C_3N_4 is illustrated in Fig. 10c. The performance of unmodified $BiVO_4$ is enhanced by a factor of ~2 and ~4 times on $TiO_2/BiVO_4$ and g-$C_3N_4/BiVO_4$, respectively. The photocurrent of bare TiO_2 is negligible as a consequence of its large band gap which hinders the efficient absorption of sunlight. So is insignificant the photocurrent of bare g-C_3N_4 due to its high recombination (Fig. 9), rendering ineffective the transport of photogenerated electron-hole pairs [72]. Fig. 10d displays the chopped photocurrent response of $TiO_2/BiVO_4$ and g-$C_3N_4/BiVO_4$, indicating both samples' quick response to input light.

The stability of $TiO_2/BiVO_4$ and g-$C_3N_4/BiVO_4$ was tested under light for 35 min at 0.6 V vs. Ag/AgCl (Fig. 11). The sharp rise of photocurrent, immediately ensued by its sudden plunge, was observed for both samples due to excitation of electrons followed by the relaxation
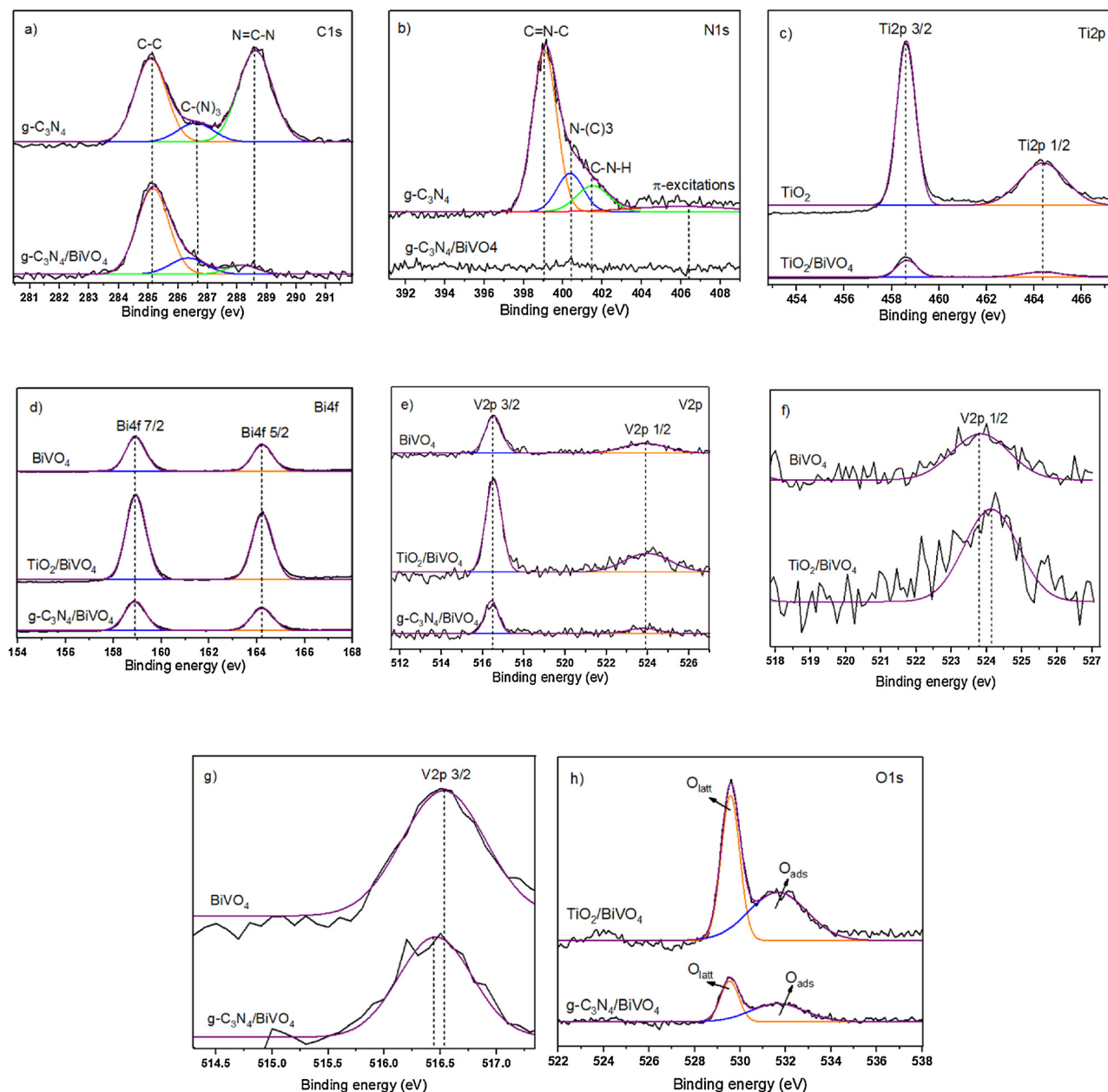
Fig. 7. XPS peaks of C1s and N1s for g-C$_3$N$_4$ and g-C$_3$N$_4$/ BiVO$_4$ (a, b), Ti2p peaks for TiO$_2$ and TiO$_2$/BiVO$_4$ (c), Bi4f and V2p peaks for BiVO$_4$, TiO$_2$/BiVO$_4$ and g-C$_3$N$_4$/ BiVO$_4$ (d, e), zoomed V2p 1/2 peaks of BiVO$_4$ and TiO$_2$/BiVO$_4$ (f), zoomed V2p 3/2 peaks of BiVO$_4$ and g-C$_3$N$_4$/ BiVO$_4$ (g) and O1s peaks for TiO$_2$/BiVO$_4$ and g-C$_3$N$_4$/ BiVO$_4$ (h).

a) TiO$_2$/ BiVO$_4$ Type (I) heterojunction b) g-C$_3$N$_4$/ BiVO$_4$ Type (II) heterojunction
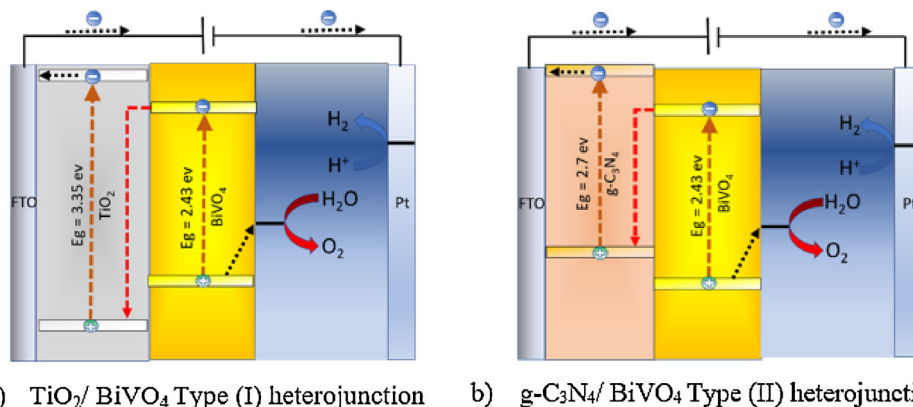
Fig. 8. The band diagram of (a) TiO$_2$/BiVO$_4$ type (I) heterojunction and (b) g-C$_3$N$_4$/BiVO4 type (II) heterojunction.
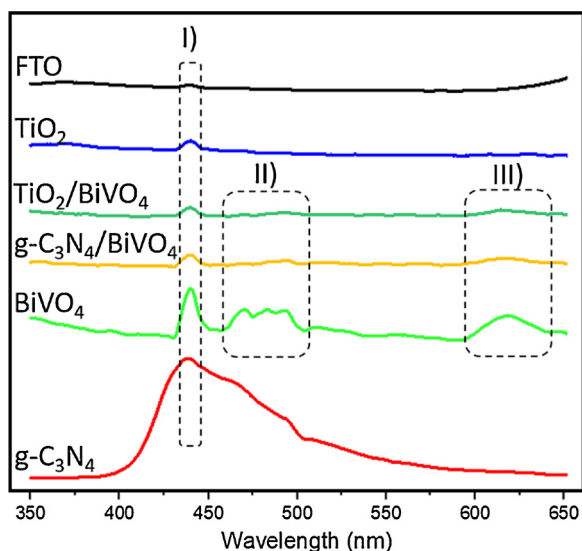
Fig. 9. Photoluminescence spectra of reference FTO (a), TiO$_2$ (b), TiO$_2$/BiVO$_4$ (c), g-C$_3$N$_4$/BiVO$_4$ (d), BiVO$_4$ (e), and g-C$_3$N$_4$ (f) thin films deposited on FTO.

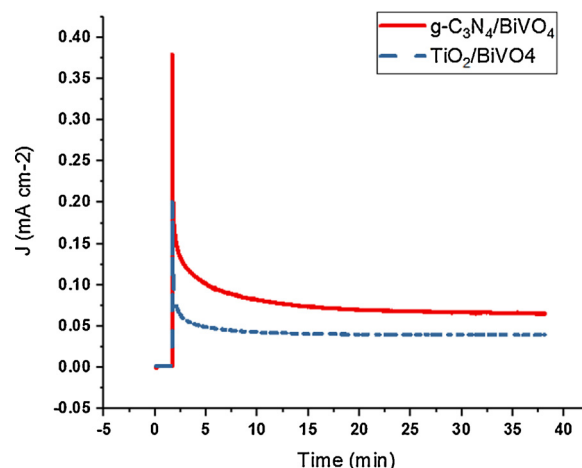**Fig. 11.** Stability test of photoanodes under illumination for 35 min in 0.5 M Na$_2$SO$_4$ under 100 mW/cm^2 of light intensity at 0.6 V vs. Ag/Agcl.

toward the conduction band. Stable photocurrent was then achieved with small decay, attributable to the slow accumulation of holes reducing charge transfer kinetics, that can be further improved with the addition of OER catalyst [22]. TiO$_2$/BiVO$_4$ indicates a steady state
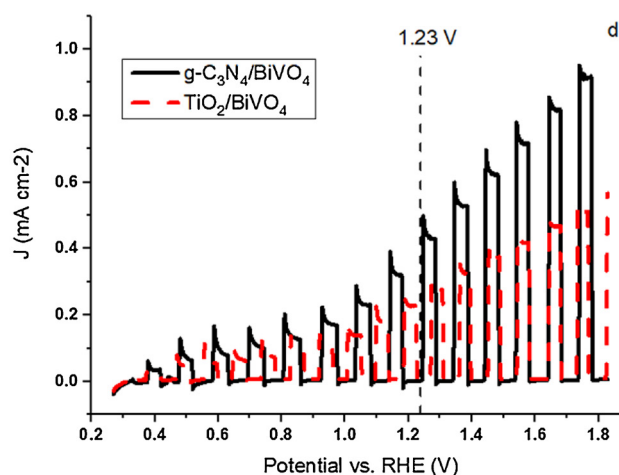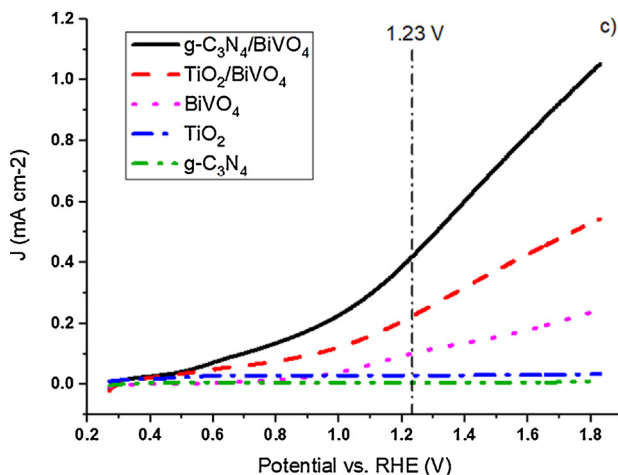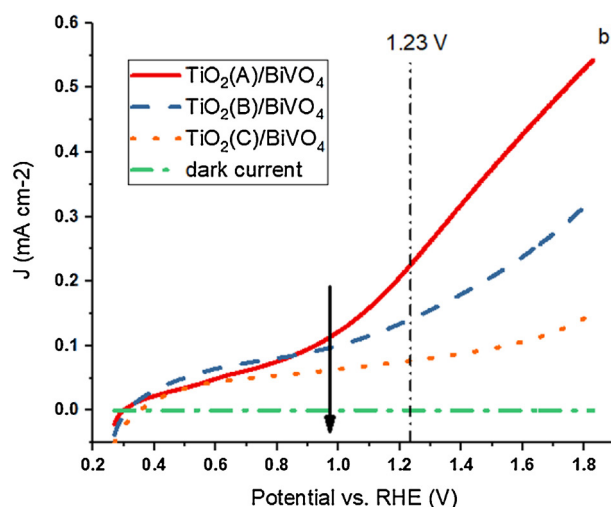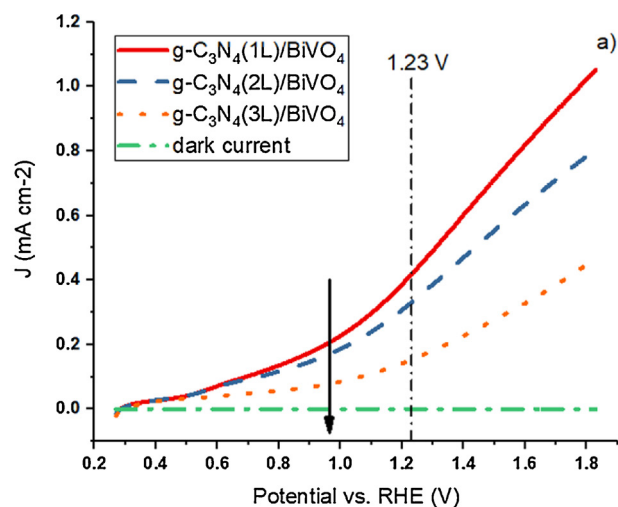
Fig. 10. LSV response of g-C$_3$N$_4$/BiVO$_4$ heterojunction (a), TiO$_2$/BiVO$_4$ heterojunction (b), bare and optimized heterojunctions photoanodes (c) and g-C$_3$N$_4$/BiVO$_4$ and TiO$_2$/BiVO$_4$ heterojunction photoanodes under chopped illumination (d). All the tests were conducted in 0.5 M Na$_2$SO$_4$ under 100 mW/cm^2 of light intensity.
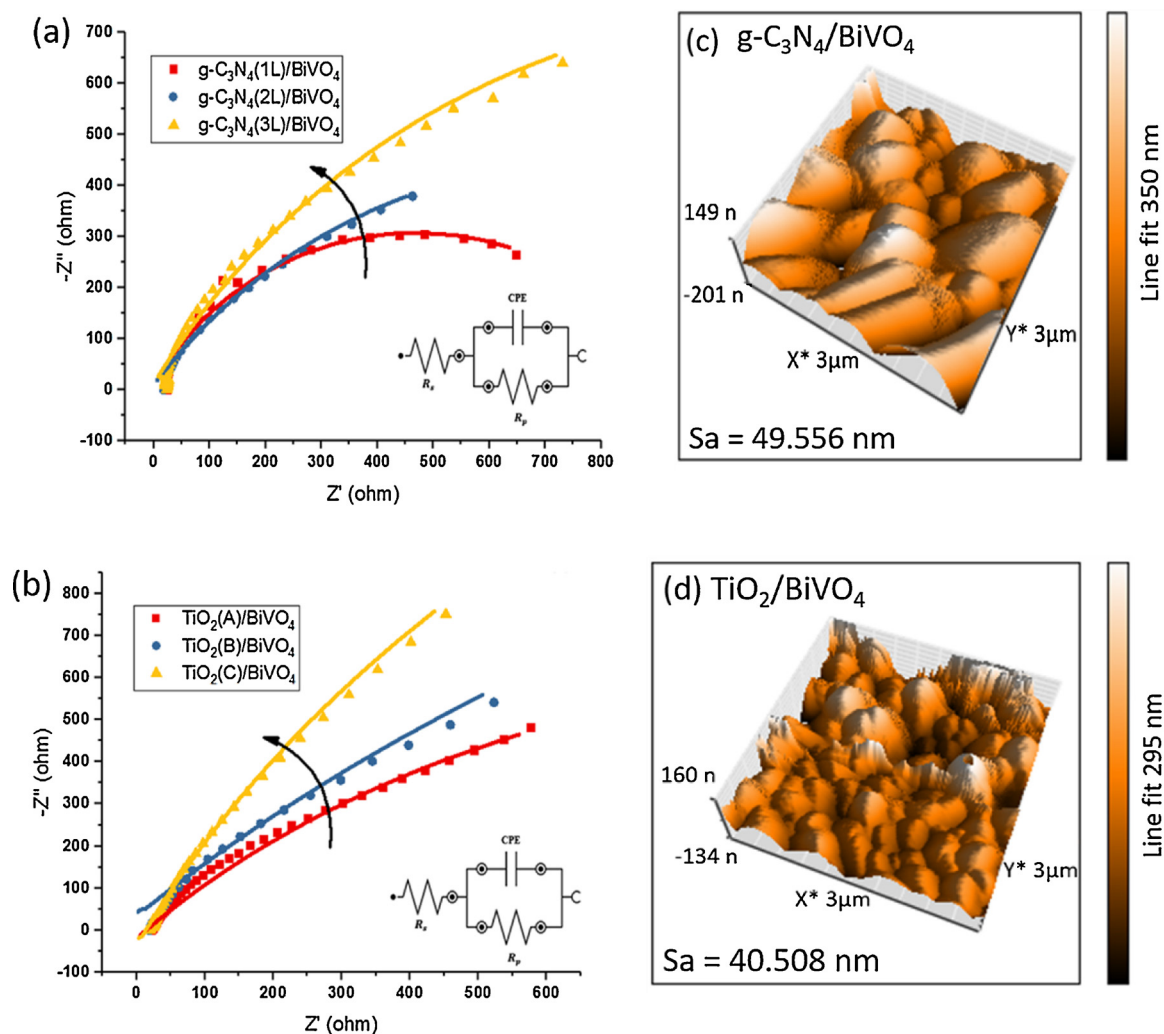
Fig. 12. EIS Nyquist plots for g-C$_3$N$_4$/BiVO$_4$ (a) and TiO$_2$/BiVO$_4$ (b). AFM result and its associated values for surface roughness (Sa) for g-C$_3$N$_4$/BiVO$_4$ (c) and TiO$_2$/BiVO$_4$(d). The higher surface roughness of g-C$_3$N$_4$/BiVO$_4$ results in its higher double layer capacitance compared with TiO$_2$/BiVO$_4$.

photocurrent after 10 min while g-C$_3$N$_4$/BiVO$_4$ demonstrates a steady state photocurrent after 30 min. From 30 to 35 min both samples showed little degredation of about 1 μA (from 65 to 64 μA) and (from 40 to 39 μA) for g-C$_3$N$_4$/BiVO$_4$ and TiO$_2$/BiVO$_4$, respectively. The results suggest that both photoanodes are highly stable in the aqueous electrolyte for long time operation.

The superior performacne of g-C$_3$N$_4$ to TiO$_2$ was substantiated by Electrical Impedance Spectroscopy (EIS) test conducted under light from 100 kHz to 10 Hz, utilizing 10 mV sinusoidal voltage at DC bias of 1 V vs. RHE. As can be observed from Fig. 12a–b, the increase in Nyquist plot radius with the increase of g-C$_3$N$_4$ or TiO$_2$ thickness, highly accorded with the results of LSV (Fig. 10a–b) where less
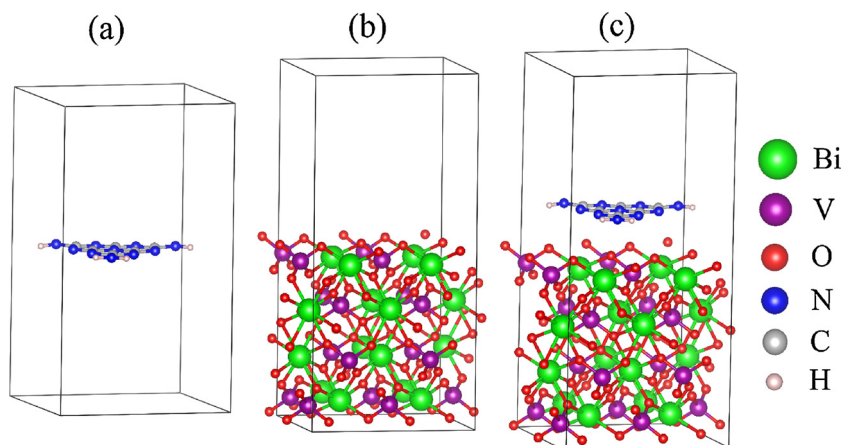

Fig. 13. Relaxed geometries of g-C$_3$N$_4$ (a), BiVO$_4$(001) (b) and g-C$_3$N$_4$/BiVO$_4$ (c).

Table 1
EIS parameters conducted at 0.6 V vs. Ag/AgCl for g-C_3N_4(1 L)/$BiVO_4$ and TiO_2(1 L)/$BiVO_4$ photoanodes.

Sample	Rs (Ω)	Rp (Ω)	CPE (μF)
g-C_3N_4(1L)/$BiVO_4$	22.81	973.7	1.01-E-05
TiO_2(A)/$BiVO_4$	23.79	2428.2	6.55-E-06

photogenerated electrons were produced for thicker layers of TiO_2 and g-C_3N_4.

Electrochemical circuit fitting was perfomred with the employment of Randles equivalent circuit. The results are presented in Table 1. The higher values of double layer capacitance or Constant Phase Element (CPE) for g-C_3N_4/$BiVO_4$, compared with TiO_2/$BiVO_4$, were due to more active photocatalytic sites for water redox reaction. This is because high surface roughness was calculated from topological images obtained from Atomic Force Microscopy (AFM) of g-C_3N_4/$BiVO_4$ compared with TiO_2/$BiVO_4$, which act as trapping centres [73] (Fig. 12c–d).

The smaller values of Rp (charge transfer resistance) for g-C_3N_4/$BiVO_4$, compared with TiO_2/$BiVO_4$, are illustrative of less charge transfer resistance between photoelectrode and electrolyte, for more oxygen vacancy sites exist on g-C_3N_4/$BiVO_4$ in comparison with those of TiO_2/$BiVO_4$. Oxygen vacancy sites make additional chemisorption between water molecules and photoelectrode, thus reducing the charge transfer resistance. Besides, Mott-Schottky test (Fig. S8) demonstrated 3.18 times higher charge carrier density for g-C_3N_4/$BiVO_4$ compared with TiO_2/$BiVO_4$, confirming a more enchanced charge carrier mobility. Other factors contributing to superior carrier mobility are the low lattice missmatch between g-C_3N_4 and $BiVO_4$ as well as an additional non-covalent bonding between Bi—N, O—C, and O—N, further elaborated in Section 3.8. The higher light absroption for g-C_3N_4/$BiVO_4$ compared with that of TiO_2/$BiVO_4$ also contributes to the Rp, for a higher number of photogenerated electrons can participate in redox reactions.

Even though both g-C_3N_4/$BiVO_4$ and TiO_2/$BiVO_4$ formed Z-scheme structure under the application of a positive bias, g-C_3N_4 demonstrated a superior PEC performance compared with that of TiO_2 as electron extraction layer to enhance the performance of $BiVO_4$. This resulted from the more negative conduction band of g-C_3N_4 (−1.72 V vs. RHE) compared with TiO_2 (−1.2 V vs. RHE) that generates a higher potential energy for water reduction (Fig. S7). Compared with TiO_2/$BiVO_4$, higher light absorption at less than 500 nm for g-C_3N_4/$BiVO_4$ produces more photogenerated electrons/holes. Higher surface roughness and the existence of V^{4+}, which induces oxygen vacancy, enhance the active catalytic sites and charge carrier mobility (see Fig. S9 in Supporting information). The doping of g-C_3N_4 to develop p-type semiconductor [74] and its incorporation with solid state mediators in p–n junction [75] are highly promising approaches that can be utilized to enhance the performance of g-C_3N_4/$BiVO_4$ photoanode.

3.8. Electronic properties of $BiVO_4$(001), g-C_3N_4, and g-C_3N_4/$BiVO_4$(001)

Drawing upon the experimental results already demonstrated in this paper, we affirm that g-C_3N_4/$BiVO_4$ heterojunction is superior to TiO_2/$BiVO_4$. To further corroborate our observations, periodic DFT calculations were performed for $BiVO_4$(001), g-C_3N_4, and g-C_3N_4/$BiVO_4$(001) heterostructure. Moreover, TiO_2/$BiVO_4$(001) heterojunction proved to possess a larger lattice mismatch (7.3%) compared with g-C_3N_4/$BiVO4$ (0.02%) (see Fig. S10 of the Supporting information). The optimized structures and lattice parameters of monolayer g-C_3N_4, bulk g-C_3N_4, $BiVO_4$, $BiVO_4$(001), and g-C_3N_4/$BiVO_4$(001) are displayed in Fig. 13 and Table S2, respectively. As discussed previously [22,76], the $BiVO_4$(001) surface is stable and nonpolar which further confirms its positive surface formation energy of 1.95 J/m^2. As a consequence of this stability, $BiVO_4$(001) slab was selected to construct g-C_3N_4/

$BiVO_4$(001) heterostructure by placing a single layer of g-C_3N_4 on the top of $BiVO_4$(001) slab (Fig. 13c). The lattice mismatch in the heterojunction of g-C_3N_4/$BiVO_4$(001) proved considerably negligible (0.02%) due to similar surface areas of $BiVO_4$(001) and monolayer g-C_3N_4 (Table S2). Hereafter, the g-C_3N_4/$BiVO_4$(001) will be referred to as g-C_3N_4/$BiVO_4$. Relaxed crystal structures of $BiVO_4$ slab and its heterojunction as well as those of g-C_3N_4 bulk and monolayer are demonstrated in Fig. S11 of the Supporting information.

A 10 Å vacuum region was employed to minimize the interactions between the neighbouring systems of g-C_3N_4/$BiVO_4$ heterojunction. The g-C_3N_4 formed a non-covalent type interaction with the surface of $BiVO_4$ through Bi—N, O—C, and O—N with simulated distances of 3.10, 2.95, and 3.12 Å, respectively which reveals strong electrostatic interaction between them. The calculated adsorption energy of g-C_3N_4 nanosheet over the $BiVO_4$(001) was −0.68 eV which confirmed the thermodynamic stability of g-C_3N_4/$BiVO_4$ heterojunction. The adsorption or interface adhesion formation energy was calculated via Eq. (2).

$$\Delta E_{ad} = E_{g\text{-}C3N4/BiVO4(001)} - (E_{g\text{-}C3N4} + E_{BiVO4(001)}) \qquad (2)$$

where $E_{g\text{-}C3N4/BiVO4(001)}$, $E_{g\text{-}C3N4}$, and $E_{BiVO4(001)}$ represent respectively the total energy of the relaxed g-$_3N_4$/$BiVO_4$(001) heterojunction, monolayer g-C_3N_4, and $BiVO_4$(001) slab. The adsorption/interface binding energy between the g-C_3N_4 monolayer and the $BiVO_4$(001) of the heterostructure (−0.68 eV) predicts strong electrostatic interaction. To corroborate the experimental high photocatalytic activity of the g-C_3N_4/$BiVO_4$(001) heterostructure, the electronic properties such as band structure and DOS of g-C_3N_4/$BiVO_4$(001) heterostructure were calculated. The energy bands of single layer g-C_3N_4 and $BiVO_4$(001) surface were also calculated for comparison (Fig. 14). The simulated band gap of $BiVO_4$(001) was 2.46 eV, consistent with our experimentally observed band gap.

Monolayer g-C_3N_4 has an indirect band gap (2.70 eV) [30] where the valence band maximum (VBM) is located at Γ point and the conduction band minimum (CBM) is at C point (Fig. 14b). The g-C_3N_4/$BiVO_4$ heterostructure has an indirect gap (2.46 eV), and the VBM is located between B and Γ points, whereas the CBM is at Γ point (see Fig. 14c). Upon interaction of g-C_3N_4 with $BiVO_4$(001), flat bands are produced in the VB of the resulted heterojunction. These flat bands are responsible for the VB of heterojunction which consequently leads to holes trapping. The enhanced overall photocatalytic activity or high charge carrier mobility can be attributed to these flat bands (vide supra). Moreover, C and N atoms of monolayer g-C_3N_4 are responsible for these flat bands (vide infra). The effective masses of the photogenerated electrons (m_e^*) and holes (m_h^*) are estimated from the band structure along suitable directions of k-points by fitting parabolic approximation around the bottom of the CBM or the top of the VBM, respectively. The Eq. (3) is employed for the calculation of these photocarriers, where $\hbar$ is the reduced Planck constant and E is the energy of an electron at wave vector k in the same band (VBM or CBM).

$$m^* = \hbar^2 \, (d^2 E / dk^2)^{-1} \qquad (3)$$

Using meta-GGA, the simulated values of the effective masses of photogenerated electrons and holes of the $BiVO_4$ slab are 0.02 and 0.01 m_e, respectively (Table 2). These masses are comparatively lower than those in our previous report, utilizing LDA method [22,76]. Although pristine $BiVO_4$ has lighter effective masses of photocarriers, responsible for high carrier mobilities, its CBM (−4.57 eV) is situated at more negative potential (vs vacuum) than the reduction potential of water (−4.5 eV).

To probe the contribution of individual species (atoms), responsible for VBM and CBM, Partial Density of State (PDOS) of these three constituents were calculated, illustrated in Fig. 15a–c. The VBM and CBM of monolayer g-C_3N_4, $BiVO_4$(001), and g-C_3N_4/$BiVO_4$ heterojunction were simulated from the DOS calculations. Fig. 15a portrays how VBM of $BiVO_4$(001) is constructed by 2p orbitals of O atoms, situated at
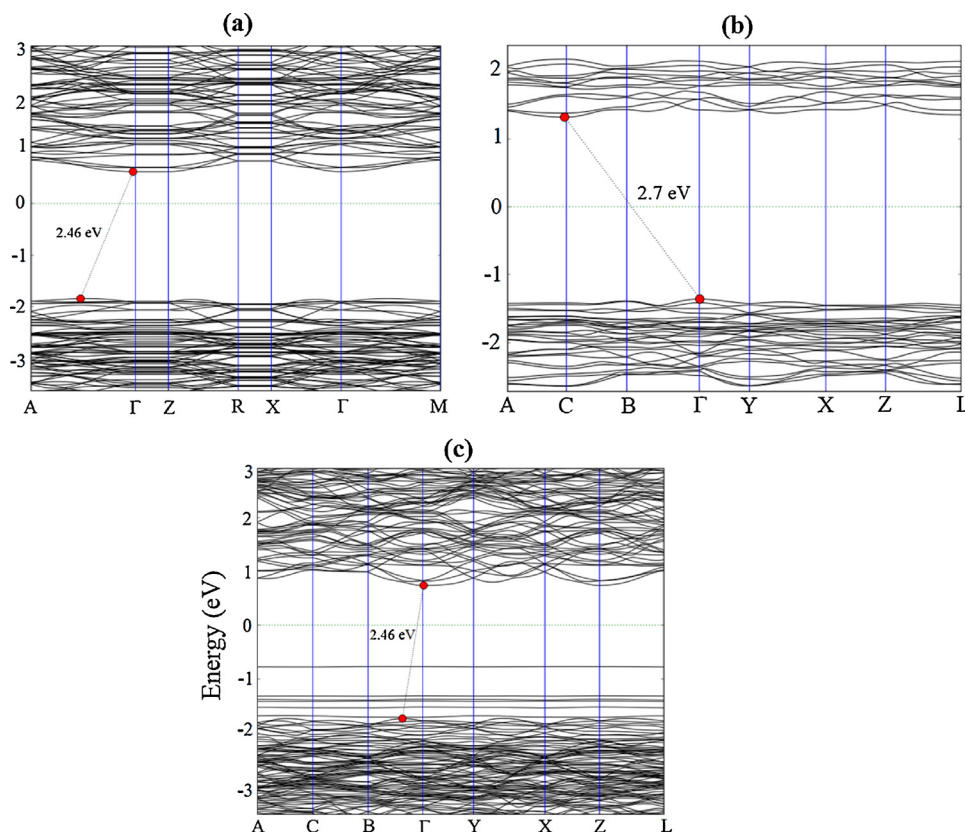
Fig. 14. Simulated band structures of BiVO$_4$(001) slab (a), g-C$_3$N$_4$ (b) and g-C$_3$N$_4$/BiVO$_4$ heterojunction (c); Fermi energy is set to zero.

Table 2
Work function, VBM, and CBM at vacuum level, band gap (in unit of eV), and effective masses of photogenerated electrons and holes; estimated from the calculated band structure along the suitable direction.

Species	Work function	m_e^*/m_0 (m$_e$)	m_h^*/m_0 (m$_e$)	VBM	CBM	Band Gap
BiVO$_4$(001)	5.18	0.02	0.01	−7.03	−4.57	2.46
g-C$_3$N$_4$	4.38	0.12	0.44	−5.74	−3.07	2.70
g-C$_3$N$_4$/BiVO$_4$	4.43	0.01	0.10	−6.16	−3.70	2.46

−7.03 eV (vs vacuum) while its CBM (−4.57 eV vs vacuum) is comprised of 5d orbitals of V atom. Furthermore, while VB of BiVO$_4$(001) is principally composed of O orbitals, its bottom section is comprised of equal contributions of V and Bi orbitals. CB of BiVO$_4$(001) is majorly composed of the anti-bonding orbitals of V atoms while its lower density section is made up of hybridized orbitals of O and Bi atoms. Both VB and CB of g-C$_3$N$_4$ are almost equally occupied by the N and C orbitals, where the VBM and CBM are situated at −5.74 and −3.07 eV (vs vacuum), respectively.

Figs. S12–S20 (Supporting information) presents the detailed contribution of s, p, and d orbitals in making VBs and CBs of these three different constituents. For the g-C$_3$N$_4$/BiVO$_4$ heterojunction, the VB (in the range of −5 to −6 eV) is chiefly occupied by N and C orbitals of g-C$_3$N$_4$ whereas the CB is dominated by the 5d anti-bonding orbitals of V of BiVO$_4$ (Fig. 15c). At vacuum level, both VBM and CBM of g-C$_3$N$_4$/BiVO$_4$ heterojunction are situated at −6.16 and −3.70 eV, respectively. Both experimental and theoretical results verify each other. Comparative analyses of VBM and CBM of the heterojunction with those of its individual constituents attest that these are respectively well below and above of the redox potential of water. Table 2 and Fig. 16 demonstrate VBM of BiVO$_4$(001) is higher than that of g-C$_3$N$_4$, whereas the CBM of g-C$_3$N$_4$ is lower than that of BiVO$_4$(001). In the resulted heterojunction, both Fermi energy and band edge positions are between

those of g-C$_3$N$_4$ and BiVO$_4$(001).

According to Fig. 16, VB and CB of heterojunction are shifted downward compared with g-C$_3$N$_4$, while these bands are shifted upward when compared with BiVO$_4$(001). Moreover, the changes in VB, CB, and Fermi energy result in band bending facilitating electron transfer [34], responsible for the enhanced photogenerated electrons. The photogenerated electrons from CB of g-C$_3$N$_4$ directly reduce water and produce H$_2$ while holes at VB of BiVO$_4$ directly oxidize water and generate O$_2$. Electrons from CB of BiVO$_4$ recombine with the holes from the VB of g-C$_3$N$_4$. The photocatalytic performance of heterojunction proved experimentally higher than that of individual g-C$_3$N$_4$ and BiVO$_4$. The enhanced performance was due to the combined band off ;set and built-in electric field that effectively transport the electrons and holes.

Fig. 16 demonstrates that CB edge position of heterojunction is more positive than that of H$^+$/H$_2$ (vs vacuum), thereby efficiently reducing H$^+$ to H$_2$. On the contrary, VB edge position of heterojunction proved more negative than that of g-C$_3$N$_4$ and positive in relation to BiVO$_4$. VB edge position of heterojunction is, in other words, at ideal position to perform oxygen evolution reaction (O$_2$/H$_2$O). Once a heterojunction is constructed, both Fermi level and the CB and VB of the resulted g-C$_3$N$_4$/BiVO$_4$ heterostructure are at diverse positions compared with those of their constituents. In brief, one can observe that g-C$_3$N$_4$/BiVO$_4$ heterojunction is a Type-II band alignment structure with lighter effective masses of electrons (0.01 m_e) and holes (0.10 m_e), responsible for high photocatalytic activities.

The inter-charge transfer at the g-C$_3$N$_4$/BiVO$_4$ heterojunction was calculated from the charge density difference (CDD) of the g-C$_3$N$_4$/BiVO$_4$ heterostructure, with the results presented in Fig. 17 where the green and yellow shaded areas represent charge accumulation and depletion, respectively. Fig. 17 also demonstrates that charge distribution principally occurs at the interface region of g-C$_3$N$_4$/BiVO$_4$ heterostructure, whereas almost no change was observed in the rest of BiVO$_4$(001), specifically in areas remote from the interface. This type of
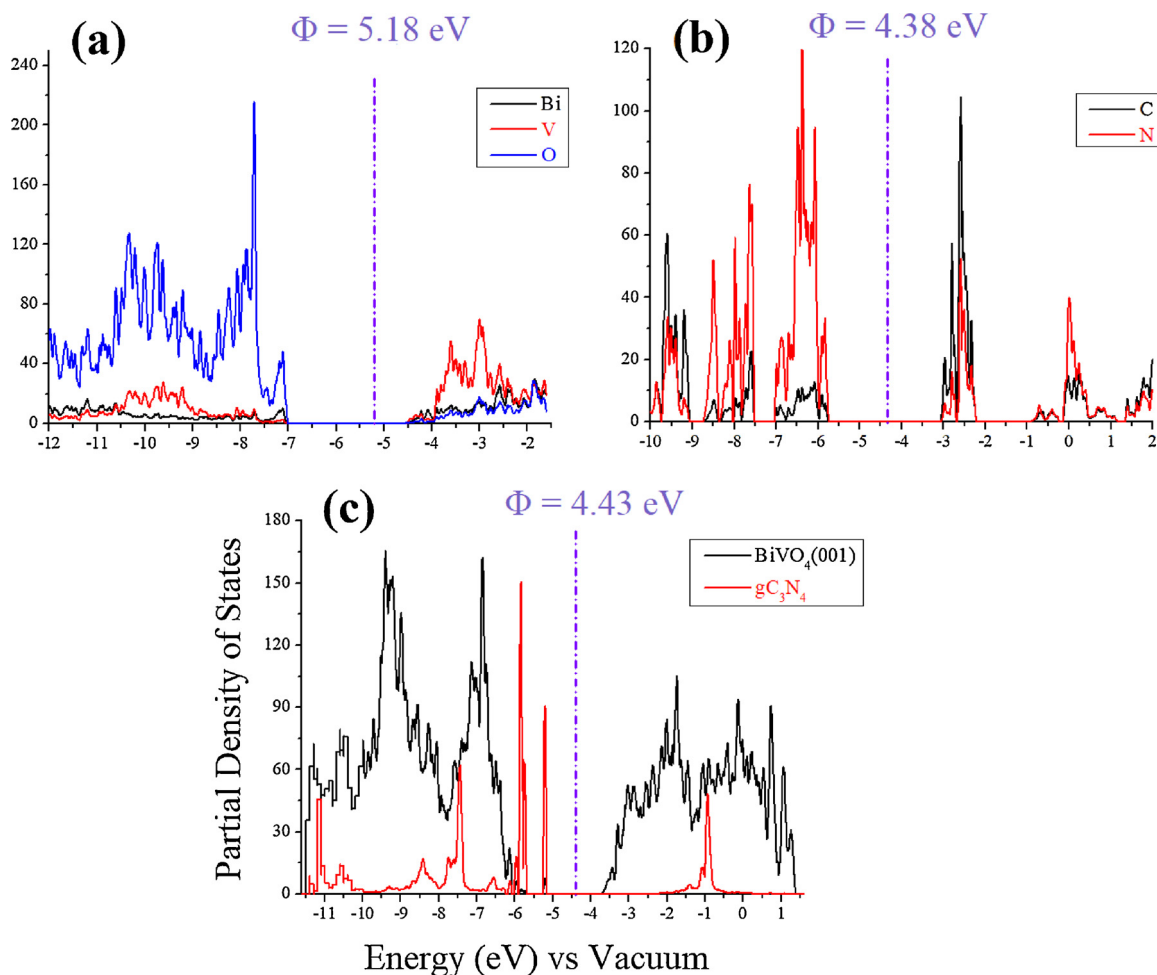
Fig. 15. PDOS plots of BiVO$_4$(001) (a), g-C$_3$N$_4$ (b) and g-C$_3$N$_4$/BiVO$_4$ (c) heterojunction. The vertical dashed lines represent the work function versus vacuum.
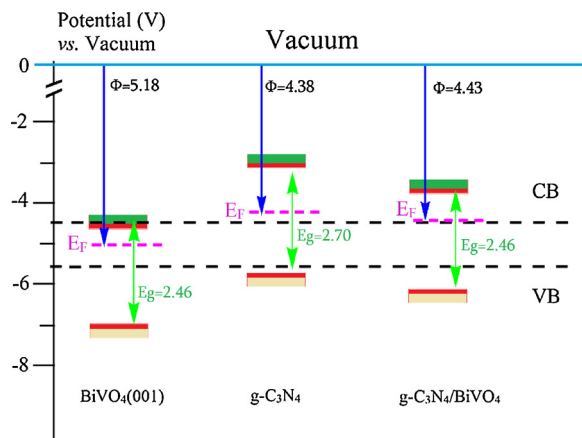
Fig. 16. Energy level diagram of the band edge positions of BiVO$_4$(001), g-C$_3$N$_4$ and g-C$_3$N$_4$/BiVO$_4$.

Fig. 17. Average electron density diff ;erence (Δρ) along Z-direction for g-C$_3$N$_4$/BiVO$_4$. The green and yellow shaded areas indicate electron accumulation and donation, respectively. (For interpretation of the references to colour in this figure legend, the reader is referred to the web version of this article.)

charge distribution may result in a weak Vander Waals type interaction [77] between g-C$_3$N$_4$ and BiVO$_4$(001), analogous to the charge distribution of a typical p−n junction [78]. Furthermore, a slice of the planar-averaged CDD along Z direction is depicted in Fig. 17 while that of pristine BiVO$_4$(001) is presented, for the sake of comparison, in Fig. S21 of the Supporting information. The charge redistribution at the interface of g-C$_3$N$_4$/BiVO$_4$ heterostructure attests that the electrons at CB of g-C$_3$N$_4$ directly reduce water while its holes recombine with the excited electrons of BiVO$_4$. In this process, holes at VB of BiVO$_4$ oxidize
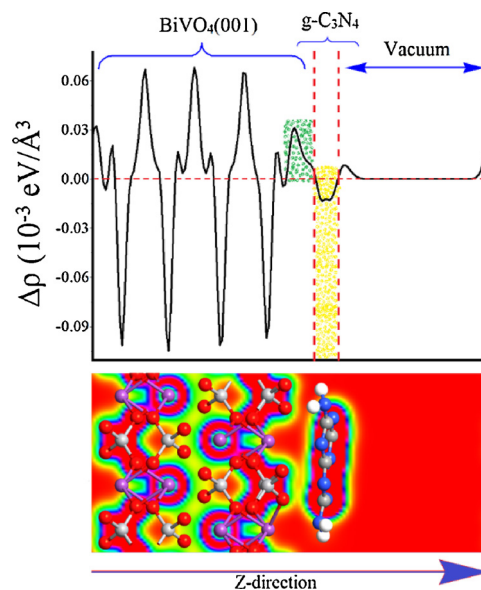
Fig. 18. Electrostatic potential maps of monolayer g-C$_3$N$_4$ (a), BiVO$_4$(001) (b) and g-C$_3$N$_4$/BiVO$_4$ heterojunction (c). The red dashed lines represent Fermi energy level, blue denotes vacuum energy level and the green dashed circle highlights the interface of g-C$_3$N$_4$/BiVO$_4$ heterojunction. (For interpretation of the references to colour in this figure legend, the reader is referred to the web version of this article.)
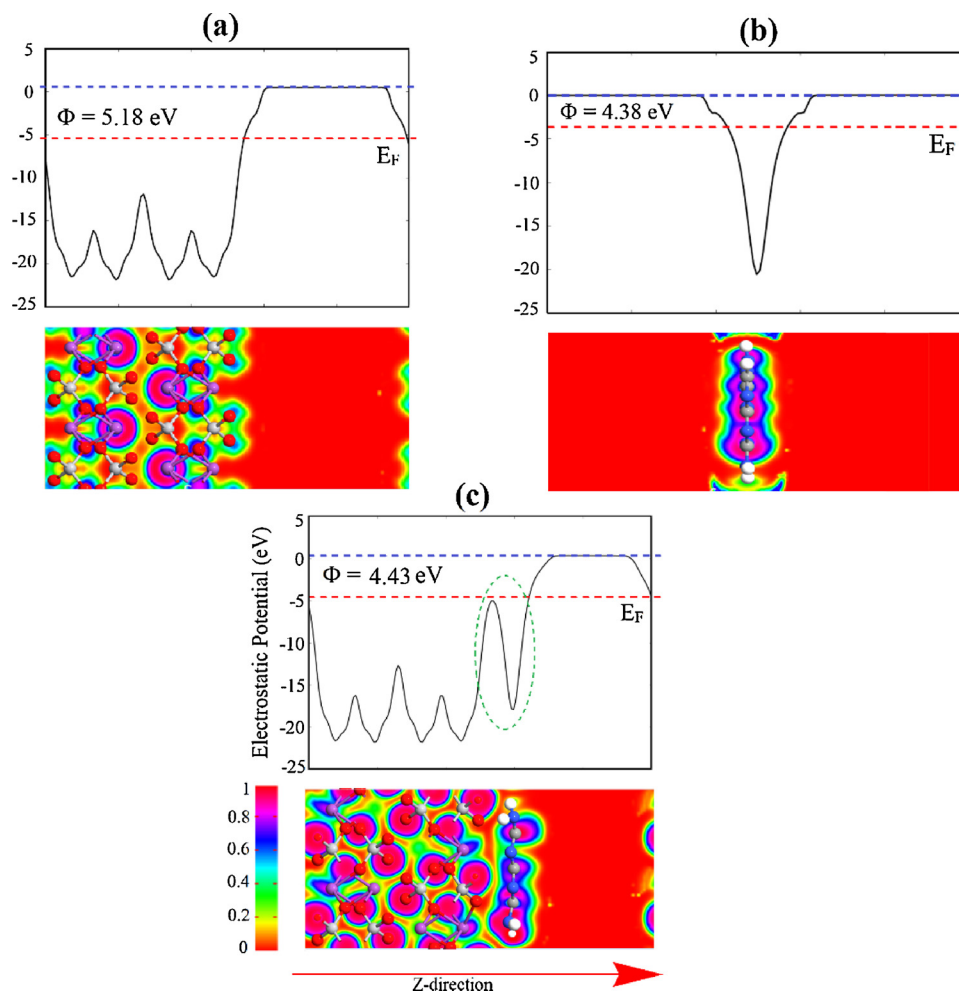
water to germinate O$_2$. The quantity of charge density difference is calculated (about 0.056 electrons) via Bader charge analysis of g-C$_3$N$_4$/BiVO$_4$ heterostructure. This charge accumulation and donation generates an electric field at the interface of g-C$_3$N$_4$/BiVO$_4$ heterostructure which further exerts the separation of electrons and holes (vide supra).

The band alignment of BiVO$_4$(001), g-C$_3$N$_4$ and g-C$_3$N$_4$/BiVO$_4$ heterojunction were calculated from the difference of E_{vac} (energy of a stationary electron in the vacuum near by the surface) and Fermi energy level (E_F), using Eq. (4).

$$\Phi = E_{vac} - E_F \qquad (4)$$

The calculated electrostatic potential maps of BiVO$_4$(001), g-C$_3$N$_4$, and g-C$_3$N$_4$/BiVO$_4$ heterojunction along Z-direction are displayed in Fig. 18 and Table 2, with simulated work functions of BiVO$_4$(001), g-C$_3$N$_4$, and g-C$_3$N$_4$/BiVO$_4$ heterojunction being 5.18, 4.38, and 4.43 eV, respectively. The diff ;erence in work function and band edge potentials (VB and CB) of g-C$_3$N$_4$ and BiVO$_4$(001) demonstrate that the charge can be effectively transferred from g-C$_3$N$_4$ to BiVO$_4$(001) at the interface of g-C$_3$N$_4$/BiVO$_4$ heterojunction. As indicated in Fig. 18 and Table 2, the work function of BiVO$_4$ surface (5.18 eV) is higher than that of monolayer g-C$_3$N$_4$ (4.38 eV), enforcing the charge to move from g-C$_3$N$_4$ to BiVO$_4$ until Fermi energy of these two constituents are aligned.

4. Conclusion

Z-scheme heterojunctions of g-C$_3$N$_4$/BiVO$_4$ and TiO$_2$/BiVO$_4$ were

successfully synthesized by electrodeposition of BiVO$_4$ on spin coated g-C$_3$N$_4$ and TiO$_2$ thin films, respectively. The obtained photocurrent response of g-C$_3$N$_4$/BiVO$_4$ proved nearly two times higher than that of TiO$_2$/BiVO$_4$, substantiating the superiority of g-C$_3$N$_4$ to TiO$_2$. This superiority manifested itself in various properties such as light absorption, surface roughness, and charge carrier mobility. The presence of interplanar hydrogen elements in g-C$_3$N$_4$ induced the formation of V^{4+}, elevating its charge carrier mobility. Furthermore, V^{4+} produced oxygen vacancy that acts as the centre of catalytic sites and chemisorbed species, culminating in its higher photoelectrochemical properties. The experimental observations were counterchecked with Density Functional Theory (DFT) simulations. The simulated results attested that g-C$_3$N$_4$ and BiVO$_4$ formed a van der Waals type heterojunction, where an internal electric field facilitates the separation of electron/hole pair at the g-C$_3$N$_4$/BiVO4 interface, restraining the carrier recombination. Comparative analyses of both experimental and theoretical studies affirm that the photogenerated electrons from CB of g-C$_3$N$_4$ directly reduce water while holes at VB of BiVO$_4$ directly oxidize water, with electrons from CB of BiVO$_4$ recombining with the holes from the VB of g-C$_3$N$_4$. The construction of Z-scheme based g-C$_3$N$_4$ PEC device engenders a promising field for further exploration and research.

and also for providing facilities to perform this research. H.U. acknowledges the supercomputing facilities of ESI Beowulf Cluster, University of Exeter, UK.

Appendix A. Supplementary data

References

[1] Y. Park, K.J. McDonald, K.-S. Choi, Progress in bismuth vanadate photoanodes for use in solar water oxidation, Chem. Soc. Rev. 42 (2013) 2321–2337.

[2] M.D. Rossell, P. Agrawal, A. Borgschulte, C.C. Hébert, D. Passerone, R. Erni, Direct evidence of surface reduction in monoclinic BiVO4, Chem. Mater. 27 (2015) 3593–3600.

[3] B.J. Morgan, G.W. Watson, A density functional theory + U study of oxygen vacancy formation at the (110),(100),(101), and (001) surfaces of rutile TiO2, J. Phys. Chem. C 113 (2009) 7322–7328.

[4] J. Pan, G. Liu, G.Q.M. Lu, H.M. Cheng, On the true photoreactivity order of {001}, {010}, and {101} facets of anatase TiO2 crystals, Angew. Chem. Int. Ed. 50 (2011) 2133–2137.

[5] M. Batzill, Fundamental aspects of surface engineering of transition metal oxide photocatalysts, Energy Environ. Sci. 4 (2011) 3275–3286.

[6] H.S. Park, K.E. Kweon, H. Ye, E. Paek, G.S. Hwang, A.J. Bard, Factors in the metal doping of BiVO4 for improved photoelectrocatalytic activity as studied by scanning electrochemical microscopy and first-principles density-functional calculation, J. Phys. Chem. C 115 (2011) 17870–17879.

[7] K.R. Tolod, S. Hernández, N. Russo, Recent advances in the BiVO4 photocatalyst for sun-driven water oxidation: top-performing photoanodes and scale-up challenges, Catal. Today 7 (2017) 13.

[8] Y. Li, R. Wang, H. Li, X. Wei, J. Feng, K. Liu, Y. Dang, A. Zhou, Efficient and stable photoelectrochemical seawater splitting with TiO2@g-C3N4 nanorod arrays decorated by Co-Pi, J. Phys. Chem. C 119 (2015) 20283–20292.

[9] X. Shi, H. Jeong, S.J. Oh, M. Ma, K. Zhang, J. Kwon, I.T. Choi, I.Y. Choi, H.K. Kim, J.K. Kim, Unassisted photoelectrochemical water splitting exceeding 7% solar-to-hydrogen conversion efficiency using photon recycling, Nat. Commun. 7 (2016).

[10] J.A. Seabold, K.-S. Choi, Efficient and stable photo-oxidation of water by a bismuth vanadate photoanode coupled with an iron oxyhydroxide oxygen evolution catalyst, J. Am. Chem. Soc. 134 (2012) 2186–2192.

[11] J.H. Kim, S. Han, Y.H. Jo, Y. Bak, J.S. Lee, A precious metal-free solar water splitting cell with a bifunctional cobalt phosphide electrocatalyst and doubly promoted bismuth vanadate photoanode, J. Mater. Chem. A 6 (2018) 1266–1274.

[12] Y. Park, D. Kang, K.-S. Choi, Marked enhancement in electron–hole separation achieved in the low bias region using electrochemically prepared Mo-doped BiVO4 photoanodes, Phys. Chem. Chem. Phys. 16 (2014) 1238–1246.

[13] F.F. Abdi, N. Firet, R. van de Krol, Efficient BiVO4 thin film photoanodes modified with cobalt phosphate catalyst and W-doping, ChemCatChem 5 (2013) 490–496.

[14] K.P.S. Parmar, H.J. Kang, A. Bist, P. Dua, J.S. Jang, J.S. Lee, Photocatalytic and photoelectrochemical water oxidation over metal-doped monoclinic BiVO4 photoanodes, ChemSusChem 5 (2012) 1926–1934.

[15] M. Zhou, J. Bao, Y. Xu, J. Zhang, J. Xie, M. Guan, C. Wang, L. Wen, Y. Lei, Y. Xie, Photoelectrodes based upon Mo: BiVO4 inverse opals for photoelectrochemical water splitting, ACS Nano 8 (2014) 7088–7098.

[16] S. Sun, W. Wang, D. Li, L. Zhang, D. Jiang, Solar light driven pure water splitting on quantum sized BiVO4 without any cocatalyst, ACS Catal. 4 (2014) 3498–3503.

[17] M. Xie, Z. Zhang, W. Han, X. Cheng, X. Li, E. Xie, Efficient hydrogen evolution under visible light irradiation over BiVO4 quantum dot decorated screw-like SnO2 nanostructures, J. Mater. Chem. A 5 (2017) 10338–10346.

[18] G. Xi, J. Ye, Synthesis of bismuth vanadate nanoplates with exposed {001} facets and enhanced visible-light photocatalytic properties, Chem. Commun. 46 (2010) 1893–1895.

[19] H. He, S.P. Berglund, A.J. Rettie, W.D. Chemelewski, P. Xiao, Y. Zhang, C.B. Mullins, Synthesis of BiVO4 nanoflake array films for photoelectrochemical water oxidation, J. Mater. Chem. A 2 (2014) 9371–9379.

[20] J. Li, J. Zhou, H. Hao, Z. Zhu, Silver-modified specific (040) facet of BiVO4 with enhanced photoelectrochemical performance, Mater. Lett. 170 (2016) 163–166.

[21] J. Li, J. Zhou, H. Hao, W. Li, G. Liu, Exposed specific (040) and (110) facets of BiVO4 modified with Bi2WO6 nanoparticles for enhanced photocatalytic performance, New J. Chem. 41 (2017) 6922–6927.

[22] S.N.F.M. Nasir, H. Ullah, M. Ebadi, A.A. Tahir, J.S. Sagu, M.A. Mat Teridi, New insights into Se/BiVO4 heterostructure for photoelectrochemical water splitting: a combined experimental and DFT study, J. Phys. Chem. C 121 (2017) 6218–6228.

[23] X. Zhang, B. Zhang, K. Cao, J. Brillet, J. Chen, M. Wang, Y. Shen, A perovskite solar cell-TiO2@ BiVO4 photoelectrochemical system for direct solar water splitting, J. Mater. Chem. A 3 (2015) 21630–21636.

[24] R. Tong, X. Wang, X. Zhou, Q. Liu, H. Wang, X. Peng, X. Liu, Z. Zhang, H. Wang, P.D. Lund, Cobalt-phosphate modified TiO2/BiVO4 nanoarrays photoanode for efficient water splitting, Int. J. Hydrogen Energy 42 (2017) 5496–5504.

[25] J. Resasco, H. Zhang, N. Kornienko, N. Becknell, H. Lee, J. Guo, A.L. Briseno, P. Yang, TiO2/BiVO4 nanowire heterostructure photoanodes based on type II band alignment, ACS Cent. Sci. 2 (2016) 80–88.

[26] X. Shi, I.Y. Choi, K. Zhang, J. Kwon, D.Y. Kim, J.K. Lee, S.H. Oh, J.K. Kim, J.H. Park, Efficient photoelectrochemical hydrogen production from bismuth vanadate-decorated tungsten trioxide helix nanostructures, Nat. Commun. 5 (2014) 4775.

[27] Y. Pihosh, I. Turkevych, K. Mawatari, J. Uemura, Y. Kazoe, S. Kosar, K. Makita, T. Sugaya, T. Matsui, D. Fujita, Photocatalytic generation of hydrogen by core-shell WO3/BiVO4 nanorods with ultimate water splitting efficiency, Sci. Rep. 5 (2015).

[28] P.M. Rao, L. Cai, C. Liu, I.S. Cho, C.H. Lee, J.M. Weisse, P. Yang, X. Zheng, Simultaneously efficient light absorption and charge separation in WO3/BiVO4 core/shell nanowire photoanode for photoelectrochemical water oxidation, Nano Lett. 14 (2014) 1099–1105.

[29] Q. Zeng, J. Li, L. Li, J. Bai, L. Xia, B. Zhou, Synthesis of WO3/BiVO4 photoanode using a reaction of bismuth nitrate with peroxovanadate on WO3 film for efficient photoelectrocatalytic water splitting and organic pollutant degradation, Appl. Catal. B: Environ. 217 (2017) 21–29.

[30] W.-J. Ong, L.-L. Tan, Y.H. Ng, S.-T. Yong, S.-P. Chai, Graphitic carbon nitride (g-C3N4)-based photocatalysts for artificial photosynthesis and environmental remediation: are we a step closer to achieving sustainability? Chem. Rev. 116 (2016) 7159–7329.

[31] X. Wang, K. Maeda, A. Thomas, K. Takanabe, G. Xin, J.M. Carlsson, K. Domen, M. Antonietti, A metal-free polymeric photocatalyst for hydrogen production from water under visible light, Nat. Mater. 8 (2009) 76–80.

[32] A. Naseri, M. Samadi, A. Pourjavadi, A.Z. Moshfegh, S. Ramakrishna, Graphitic carbon nitride (gC3N4)-based photocatalysts for solar hydrogen generation: recent advances and future development directions, J. Mater. Chem. A 5 (2017) 23406–23433.

[33] S. Cao, J. Low, J. Yu, M. Jaroniec, Polymeric photocatalysts based on graphitic carbon nitride, Adv. Mater. 27 (2015) 2150–2176.

[34] J. Fu, J. Yu, C. Jiang, B. Cheng, gC3N4 based heterostructured photocatalysts, Adv. Energy Mater. 8 (2017) 1701503.

[35] H. Ullah, A.A. Tahir, S. Bibi, T.K. Mallick, S.Z. Karazhanov, Electronic properties of β-TaON and its surfaces for solar water splitting, Appl. Catal. B: Environ. 229 (2018) 24–31.

[36] J. Albero, E.M. Barea, J. Xu, I. Mora-Seró, H. Garcia, M. Shalom, Toward efficient carbon nitride photoelectrochemical cells: understanding charge transfer processes, Adv. Mater. Interfaces 4 (2017).

[37] Š. Hajduk, S.P. Berglund, M. Podlogar, G. Dražić, F.F. Abdi, Z.C. Orel, M. Shalom, Conformal carbon nitride coating as an efficient hole extraction layer for ZnO nanowires-based photoelectrochemical cells, Adv. Mater. Interfaces 4 (2017).

[38] C.-H. Wang, D.-D. Qin, D.-L. Shan, J. Gu, Y. Yan, J. Chen, Q.-H. Wang, C.-H. He, Y. Li, J.-J. Quan, Assembly of gC3N4-based type II and Z-scheme heterojunction anodes with improved charge separation for photoelectrojunction water oxidation, Phys. Chem. Chem. Phys. 19 (2017) 4507–4515.

[39] K.J. McDonald, K.-S. Choi, A new electrochemical synthesis route for a BiOI electrode and its conversion to a highly efficient porous BiVO4 photoanode for solar water oxidation, Energy Environ. Sci. 5 (2012) 8553–8557.

[40] D. Kang, Y. Park, J.C. Hill, K.-S. Choi, Preparation of Bi-based ternary oxide photoanodes BiVO4, Bi2WO6, and Bi2Mo3O12 using dendritic Bi metal electrodes, J. Phys. Chem Lett. 5 (2014) 2994–2999.

[41] C.K. Gupta, T. Mukherjee, Hydrometallurgy in Extraction Processes, CRC Press, 1990.

[42] J.H. Kim, G. Magesh, H.J. Kang, M. Banu, J.H. Kim, J. Lee, J.S. Lee, Carbonate-coordinated cobalt co-catalyzed BiVO4/WO3 composite photoanode tailored for CO2 reduction to fuels, Nano Energy 15 (2015) 153–163.

[43] AtomistixToolKit, version 2017.1, QuantumWise A/S, (www.quantumwise.com).

[44] VirtualNanoLab, version 2017.1, QuantumWise A/S, (www.quantumwise.com).

[45] A. Sleight, H.-Y. Chen, A. Ferretti, D. Cox, Crystal growth and structure of BiVO 4, Mater. Res. Bull. 14 (1979) 1571–1581.

[46] A.H. Larsen, M. Vanin, J.J. Mortensen, K.S. Thygesen, K.W. Jacobsen, Localized atomic basis set in the projector augmented wave method, Phys. Rev. B 80 (2009) 195112.

[47] G. Kresse, D. Joubert, From ultrasoft pseudopotentials to the projector augmented-wave method, Phys. Rev. B 59 (1999) 1758.

[48] F. Tran, P. Blaha, Accurate band gaps of semiconductors and insulators with a semilocal exchange-correlation potential, Phys. Rev. Lett. 102 (2009) 226401.

[49] J. Endres, D.A. Egger, M. Kulbak, R.A. Kerner, L. Zhao, S.H. Silver, G. Hodes, B.P. Rand, D. Cahen, L. Kronik, Valence and conduction band densities of states of metal halide perovskites: a combined experimental–theoretical study, J. Phys. Chem. Lett. 7 (2016) 2722–2729.

[50] E. Muniz, M. Goes, J. Silva, J.A. Varela, E. Joanni, R. Parra, P.R. Bueno, Synthesis and characterization of mesoporous TiO2 nanostructured films prepared by a modified sol–gel method for application in dye solar cells, Ceram. Int. 37 (2011) 1017–1024.

[51] D. Kang, T.W. Kim, S.R. Kubota, A.C. Cardiel, H.G. Cha, K.-S. Choi, Electrochemical synthesis of photoelectrodes and catalysts for use in solar water splitting, Chem. Rev. 115 (2015) 12839–12887.

[52] J.H. Kim, Y.H. Jo, J.H. Kim, J.S. Lee, Ultrafast fabrication of highly active BiVO4 photoanodes by hybrid microwave annealing for unbiased solar water splitting, Nanoscale 8 (2016) 17623–17631.

[53] B.-Y. Cheng, J.-S. Yang, H.-W. Cho, J.-J. Wu, Fabrication of an efficient BiVO4–TiO2 heterojunction photoanode for photoelectrochemical water oxidation, ACS Appl. Mater. Interfaces 8 (2016) 20032–20039.

[54] Y. Qiu, W. Liu, W. Chen, G. Zhou, P.-C. Hsu, R. Zhang, Z. Liang, S. Fan, Y. Zhang, Y. Cui, Efficient solar-driven water splitting by nanocone BiVO 4-perovskite tandem cells, Sci. Adv. 2 (2016) e1501764.

[55] M. Ma, J.K. Kim, K. Zhang, X. Shi, S.J. Kim, J.H. Moon, J.H. Park, Double-deck inverse opal photoanodes: efficient light absorption and charge separation in

heterojunction, Chem. Mater. 26 (2014) 5592–5597.

[56] Y. Zhou, L. Zhang, L. Lin, B.R. Wygant, Y. Liu, Y. Zhu, Y. Zheng, C.B. Mullins, Y. Zhao, X.-H. Zhang, Highly efficient photoelectrochemical water splitting from hierarchical WO3/BiVO4 nanoporous sphere arrays, Nano Lett. 17 (2017) 8012–8017.

[57] S. Le, T. Jiang, Q. Zhao, X. Liu, Y. Li, B. Fang, M. Gong, Cu-doped mesoporous graphitic carbon nitride for enhanced visible-light driven photocatalysis, RSC Adv. 6 (2016) 38811–38819.

[58] M. Zalfani, B. van der Schueren, Z.-Y. Hu, J.C. Rooke, R. Bourguiga, M. Wu, Y. Li, G. Van Tendeloo, B.-L. Su, Novel 3DOM BiVO4/TiO2 nanocomposites for highly enhanced photocatalytic activity, J. Mater. Chem. A 3 (2015) 21244–21256.

[59] J. Jiang, J. Yu, S. Cao, Au/PtO nanoparticle-modified gC3N4 for plasmon-enhanced photocatalytic hydrogen evolution under visible light, J. Colloid Interface Sci. 461 (2016) 56–63.

[60] G. Wang, Y. Ling, X. Lu, F. Qian, Y. Tong, J.Z. Zhang, V. Lordi, C. Rocha Leao, Y. Li, Computational and photoelectrochemical study of hydrogenated bismuth vanadate, J. Phys. Chem. C 117 (2013) 10957–10964.

[61] D.-D. Qin, T. Wang, Y.-M. Song, C.-L. Tao, Reduced monoclinic BiVO4 for improved photoelectrochemical oxidation of water under visible light, Dalton Trans. 43 (2014) 7691–7694.

[62] Z. Wang, J. Lv, J. Zhang, K. Dai, C. Liang, Facile synthesis of Z-scheme BiVO 4/ porous graphite carbon nitride heterojunction for enhanced visible-light-driven photocatalyst, Appl. Surf. Sci. 430 (2017) 595–602.

[63] J.H. Kim, Y. Jo, J.H. Kim, J.W. Jang, H.J. Kang, Y.H. Lee, D.S. Kim, Y. Jun, J.S. Lee, Wireless solar water splitting device with robust cobalt-catalyzed, dual-doped BiVO4 photoanode and perovskite solar cell in tandem: a dual absorber artificial leaf, ACS Nano 9 (2015) 11820–11829.

[64] Y. Zhang, Y. Guo, H. Duan, H. Li, C. Sun, H. Liu, Facile synthesis of V4 + self-doped, [010] oriented BiVO4 nanorods with highly efficient visible light-induced photocatalytic activity, Phys. Chem. Chem. Phys. 16 (2014) 24519–24526.

[65] F. Chen, Q. Yang, X. Li, G. Zeng, D. Wang, C. Niu, J. Zhao, H. An, T. Xie, Y. Deng, Hierarchical assembly of graphene-bridged Ag3PO4/Ag/BiVO4 (040) Z-scheme photocatalyst: an efficient, sustainable and heterogeneous catalyst with enhanced visible-light photoactivity towards tetracycline degradation under visible light ir-radiation, Appl. Catal. B: Environ. 200 (2017) 330–342.

[66] M. Ye, J. Gong, Y. Lai, C. Lin, Z. Lin, High-efficiency photoelectrocatalytic hydrogen generation enabled by palladium quantum dots-sensitized TiO2 nanotube arrays, J. Am. Chem. Soc. 134 (2012) 15720–15723.

[67] T. An, J. Tang, Y. Zhang, Y. Quan, X. Gong, A.M. Al-Enizi, A.A. Elzatahry, L. Zhang,

G. Zheng, Photoelectrochemical conversion from graphitic C3N4 quantum dot de-corated semiconductor nanowires, ACS Appl. Mater. Interfaces 8 (2016) 12772–12779.

[68] S. Le, T. Jiang, Y. Li, Q. Zhao, Y. Li, W. Fang, M. Gong, Highly efficient visible-light-driven mesoporous graphitic carbon nitride/ZnO nanocomposite photocatalysts, Appl. Catal. B: Environ. 200 (2017) 601–610.

[69] S. Thaweesak, M. Lyu, P. Peerakiatkhajohn, T. Butburee, B. Luo, H. Chen, L. Wang, Two-dimensional g-C3N4/Ca2Nb2TaO10 nanosheet composites for efficient visible light photocatalytic hydrogen evolution, Appl. Catal. B: Environ. 202 (2017) 184–190.

[70] J. Su, P. Geng, X. Li, Q. Zhao, X. Quan, G. Chen, Novel phosphorus doped carbon nitride modified TiO2 nanotube arrays with improved photoelectrochemical per-formance, Nanoscale 7 (2015) 16282–16289.

[71] J. Liu, H. Wang, Z.P. Chen, H. Moehwald, S. Fiechter, R. van de Krol, L. Wen, L. Jiang, M. Antonietti, Microcontact-printing-assisted access of graphitic carbon nitride films with favorable textures toward photoelectrochemical application, Adv. Mater. 27 (2015) 712–718.

[72] M. Yan, Y. Hua, F. Zhu, L. Sun, W. Gu, W. Shi, Constructing nitrogen doped gra-phene quantum dots-ZnNb2O6/g-C3N4 catalysts for hydrogen production under visible light, Appl. Catal. B: Environ. 206 (2017) 531–537.

[73] M. Noh, F. Mohamad, M.F. Soh, M.A. Riza, J. Safaei, M. Nasir, N. Siti, M. Sapian, W. Norfaizzatul, C.H. Teh, Effect of film thickness on photoelectrochemical per-formance of SnO2 prepared via AACVD, Phys. Status Solidi (B) (2018) 1700570.

[74] L. Jiang, X. Yuan, Y. Pan, J. Liang, G. Zeng, Z. Wu, H. Wang, Doping of graphitic carbon nitride for photocatalysis: a reveiw, Appl. Catal. B: Environ. 217 (2017) 388–406.

[75] Z. Wei, D. Benlin, Z. Fengxia, T. Xinyue, X. Jiming, Z. Lili, L. Shiyin, D.Y. Leung, C. Sun, A novel 3D plasmonic pn heterojunction photocatalyst: Ag nanoparticles on flower-like p-Ag2S/n-BiVO4 and its excellent photocatalytic reduction and oxida-tion activities, Appl. Catal. B: Environ. 229 (2018) 171–180.

[76] H. Ullah, A.A. Tahir, T.K. Mallick, Structural and electronic properties of oxygen defective and Se-doped p-type BiVO4 (001) thin film for the applications of pho-tocatalysis, Appl. Catal. B: Environ. 224 (2018) 895–903.

[77] J. Liu, Origin of high photocatalytic efficiency in monolayer g-C3N4/CdS hetero-structure: a hybrid DFT study, J. Phys. Chem. C 119 (2015) 28417–28423.

[78] M. Niu, D. Cheng, D. Cao, Understanding the mechanism of photocatalysis en-hancements in the graphene-like semiconductor sheet/TiO2 composites, J. Phys. Chem. C 118 (2014) 5954–5960.